Fractured reservoirs: a comparison of different modelling approaches, from a well to reservoir and reservoir to well perspective

Rhys Coles

4231082

Msc thesis Utrecht University

Supervisor: Dr Jan Ter Heege (TNO)

Co Supervisor: Dr Maartje Houben

Table of Contents

Abstract:

Predicting the potential for successful hydraulic stimulation of shale targets in the Netherlands is key when assessing the optimum areas for well emplacement. The difficulty of assessing areas which will respond favourably to stimulation is associated with limited data sets, namely the absence of well tests and adequate case studies. Therefore, studies have attempted to build robust reservoir models which estimate the fracturing potential of the shale. We compare two modelling approaches. Firstly, an elementary modelling technique where only tensile fracturing is assumed. Secondly, we have developed a semi-analytical model which creates a synthetic natural fault network based on a power law distribution, and established a new method of spatially distributing fractures. This study analyses the petrophysical rock properties at a number of well locations penetrating the Posidonia and Geverik shales. Hydraulic fracturing simulations indicate that the uncertainty associated with leak off has a profound influence on fracture dimensions. We show that areas with a high Young's modulus are characterised by longer fractures and conclude that stimulation is likely to be most successful at well KWK-01 (near Boxtel). Results from the analytical model indicate that reactivated faults following a power law distribution also follow a Guttenberg-Richter distribution. Additionally, moment magnitudes predicted by the model are similar to those recorded during hydraulic fracturing in other studies. We use seismicity within the reservoir to calculate permeability and fluid flow. From this we recreate the reactivation of faults within the reservoir by injecting fluids until yield pressures on outermost faults are reached and record the total volume of fluid. This total fluid volume is empirically related to the cumulative seismic moment with the method of McGarr (2014). We observe a good match between model predicted seismicity and McGarr (2014) predictions showing the validity of the model. The results from the semi-analytical natural fracture model indicate that a power law distribution of faults is a meaningful way in which to represent natural fractures within reservoirs.

Introduction

The U.S.A has achieved enormous success in extracting shale gas, especially from the renowned Barnett shale in northern Texas. Subsequently, many other countries have begun to explore their potential for shale gas. The Netherlands subsurface may host potential targets for shale oil and shale gas due to Lower cretaceous lacustrine sediments, Jurassic marine organic rich marls and a range of carboniferous black shales (Bruns, et al., 2016). This study focusses on the Lower Jurassic Posidonia Shale Formation and the Carboniferous Geverik Member of the Epen Formation, situated in The Netherlands (Figure 2) and the Woodford, Barnett and Marcellus Shale. Shale gas is often labeled as an unconventional resource and is unique when compared to conventional gas resources because gas-bearing shales are synonymously the source rock and reservoir rock, in which gas exists partly as an absorbed and partly as a free component (Grieser & Bray, 2007). In order to extract gas from a shale the permeability of the rock must be increased through hydraulic fracturing. In the wake of the global oil price shock, evaluation of the efficiency of hydraulic fracturing is more important than ever in tight reservoirs to increase the chances of successful development of plays (Geng, et al., 2016). Furthermore, the cost of hydraulic fracturing is high, therefore a robust treatment design is required (Wang, et al., 2016). This research focusses on faults and fractures and leans towards low permeability shale reservoirs for two reasons. Firstly, in low permeability reservoirs the importance of fractures concerning the flow of hydrocarbons is amplified because matrix permeability is low. Secondly, there is an abundance of data concerning hydraulic fracturing and production from the

Woodford, Barnett and Marcellus Shale and a wealth of borehole data to characterise reservoir properties of the Posidonia, and to a lesser extent the Geverik.

There has been extensive modelling of the mechanical response of reservoirs to hydraulic stimulation. Warpinski et al. (2009) among others state that rock failure occurs from newly created fractures through tensile opening, slip on pre-existing fractures or a hybrid mechanism. Commercial ventures often adopt an elementary modelling approach, where the emphasis is on tensional fractures and gas flow rates are interpreted from this. In this study, we first adopt an elementary approach by using the software MFrac and simulate tensile fractures and discount reactivation of fractures in shear (mode II fractures).

Apparent from the literature is the immense complexity of fracturing due to the interaction of natural and hydraulic fractures, evident from micro seismicity (Wang, et al., 2016). This interaction is important as it influences the optimum operational parameters such as fluid viscosity, injection rate and injection volume (Wang, et al., 2016). Furthermore, the discourse of many researchers involved in shale gas exploration in the Netherlands indicates that shale gas exploitation would not have the same success as in other areas, such as the Barnett Shale. The reason for this is related to the compositional differences of both shales, the Barnet has a higher content of coarse sand layers and natural fracture density when compared to the Posidonia. The sand layers and natural fractures act as gas flow paths, increasing the permeability of the reservoir.

Another approach to modelling hydraulic fracturing is to create a natural fracture network based on geological and geophysical characterization of fracture populations, and model injection induced stress changes and fracture reactivation. Ter Heege (2016) reasons that the spatial distribution of reactivated faults and fractures and their permeability are the main parameters which control the drainage area, connectivity and hydrocarbon flow rates. Authors such as Breede et al. (2013) state that natural fractures play a key role in governing the evolution of permeability during stimulation. Thus, natural fractures can explain why in some cases production rates from shale reservoirs are much higher than elementary commercial modelling accounted for. Additionally, fracture development is more complex when accounting for interaction of natural and induced fractures (Hofmann & Babadagli, 2013). Thus, highlighting the importance of including a natural fracture network and questions the validity of elementary modelling techniques. Fischer et al (2008) state that hydraulic fracture propagation is strongly anisotropic which is controlled by the orientation of the horizontal stresses, stiffness, leak off coefficient and injection rate. Recently several studies have attempted to link fluid-flow, geomechanical and seismic models to improve prediction of how a reservoir responds to fluid extraction, stress redistribution and mechanical deformation (Verdon, et al., 2011). There have been several attempts to model fractures and their associated density, length and orientation to improve permeability estimates, thus providing a better estimate for fluid flow. This research uses the elementary approach of Mfrac and compares it with an analytical model which creates a synthetic natural fault network.

Research questions

1. What are the differences and similarities regarding the characterization of fractured reservoirs between an elementary approach and making use of a power law distribution?
2. What is the applicability of using a power law relationship for the cumulative frequency of fault sizes in models that estimate both seismic moment magnitude, and spatial distribution of fractures to characterize fluid flow?

Objectives:

1. Apply MFrac simulations to estimate the dimensions of tensile fractures following fluid injection for a number of wells intersecting the Posidonia and Geverik **Figure 2**.
2. Assess which parameters have the most profound impact on fracture properties and comment on the spatial variation in efficiency of hydraulic fracturing.
3. Create an analytical model which:
    - Generates a fault network model that honors a power law relationship for fault lengths and a weighted probability for the location of faults
    - Produces an estimate of the magnitude and location of seismic events
    - Model permeability on reactivated fractures
    - Create an elliptical stimulated reservoir volume and assess the fluid volume required to create failure within the model.
    - Compare the cumulative seismic moment to the maximum seismic moment calculated from the fluid volume (McGarr, 2014).

Scientific background

Natural and induced fractures

Mode I & II fractures

Olding et al. (1999) and Bonnet et al., (2001) consider hydrocarbon flow rates, well to reservoir connectivity and typical drainage areas and concluded that they are largely defined by the spatial distributed of faults and fractures. Gale et al. (2007) indicate that natural fractures in shales are often narrow (<0.05mm), present in echelon arrays and sealed with calcite, thus hydraulic fracturing is required to induce permeability.

The type of the fracture can have implications for the fracture initiation pressure, fracture orientation and fracture growth. In turn this affects the distribution of permeability throughout the reservoir and with this, the optimum orientation of wells. Orientation of fractures is important, those orientated optimally for failure will reactivate at lower injection pressures, i.e for a normal faulting regime the optimally orientated fractures dip towards the minimum horizontal stress. Tensile opening of fractures is controlled by the cohesive (or tensile) strength (T) of rocks with new fractures, whereas existing fractures assume a cohesive strength of 0, in the latter case failure is controlled by the friction coefficient (Wassing et al., 2014). Graphically both modes of fracture can be represented on a combined Griffith Coulomb criterion (Figure 1). Tensile opening of fractures occurs in the small, non-linear region of the strength envelope (green circle) where normal stresses are negative (Eckert, 2007) . Shear failure resides in the region where normal stresses are positive (Fischer & Guest, 2011). Both situations are discernible by the differential stress (σ_d), when σ_d>4T shear failure dominates whilst tensile opening dominates when σ_d<4T (Figure 1).

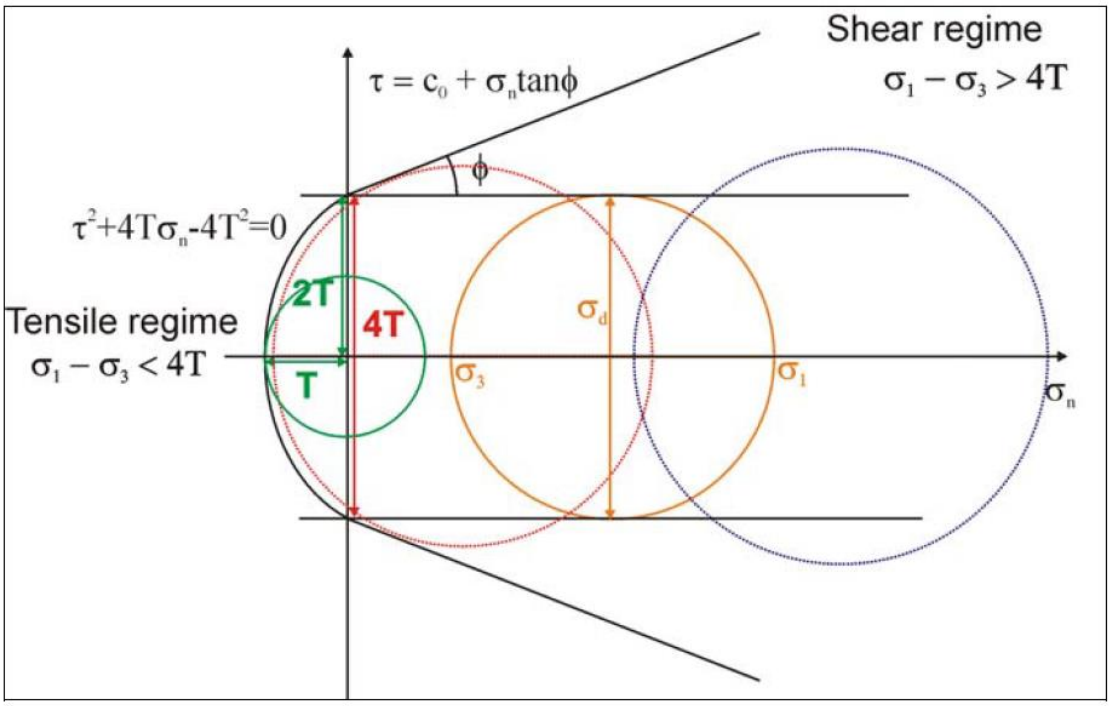

Figure 1 shows the combined Griffith - Coulomb failure criterion - shear failure is possible if σ_d>4T (blue and red circles) and tensile failure if σ_d<4T (green circle) (Eckert, 2007).

Tensile fractures form parallel to the minimum horizontal stress direction (Sh_{min}) and shear fractures perpendicular (assuming normal faults) (TerHeege, 2016). Tensile fractures will propagate in the direction of least resistance, i.e (Sh_{min}). When assuming normal faulting, failure is defined by the ratio of normal to shear stress. Fractures orientated perpendicular to the direction of Sh_{min} will have the highest ratios. In the West Netherlands basin Ter Heege et al. (2016) found that for a strike slip regime fractures were consistently orientated at 45° to the minimum horizontal stress. Breede et al (2013) state that natural fractures play a key role in governing the hydraulic evolution of the reservoir.

The complexity of fracture development stems from the interaction of natural and induced fractures where a hybrid of the two occurs (Hofmann & Babadagli, 2013). Fracture growth dominated by shear failure (mode II) will differ from those dominated by tensile failure (mode I) as both result in markedly different fracture dimensions due to the mode of opening. Wang et al (2016) state that the fluid viscosity, injection rate, injection volume and permeability are the most important parameters to consider during hydraulic stimulation as they control reservoir pressure change. Increased fluid viscosity, injection rate, volume and low permeability will favour tensile fractures as higher pressures will rapidly develop. Hence, Nearing et al (2016) argue that increasing the injection rate gradually favours the development of shear reactivation, whereas rapid increase favours tensile fractures. This is related to the dispersion of fluids; gradual injection means that fluids and importantly the pressure front will not build up as much.

Distribution of fractures

Conventionally researchers used techniques such as core samples to deduce fracture densities and attempted to correlate this data to the rest of the reservoir (Gale, et al., 2007). However, this method is limited because the it relies on borehole measurements being representative of the entire reservoir. This is problematic because of the observed spatial variability of faults in shales where fractures are often found in areas of high concentration. The use of three dimensional seismics has improved the identification of faults and fractures in the reservoir, with a resolution of 10-20m but at depths of 3km this resolution reduces to 30m (Yielding, et al., 1996). Many studies attempt to use both core samples and 3D seismics in order to constrain fracture distributions but the low resolution of 3D seismics and the fact that borehole diameters are typically 10 centimeters in diameter means that there is a data gap when attempting the characterization of faults in the reservoir.

Fault reactivation, particularly in shear resulting from fluid injection leads to the release of stored energy and seismicity. With the addition of geophones to the borehole wall, seismic arrival times can infer important information regarding the mode and distribution of fractures. Seismic moments are important when the regarding characterization of faults and fractures within the reservoir. Perhaps the most valuable use of micro-seismic data is to monitor the propagation of hydraulic fracturing (Angus, et al., 2010). It is suggested that microseismic data can not only infer spatial and temporal changes in the stress field due to injection but also characterize reservoir anisotropy (Verdon, et al., 2011). Furthermore, Angus et al. (2010) reason that microseismic data can measure the strength, orientation and type of elastic failure needed to calculate damage zones. This is relevant to this study as micro seismics provide a way of validating the characterization of faults using a power law relationship by comparing location and magnitudes of seismic moments. Studies such as Verdon et al. (2011) have inverted seismic moments from microseismic data and calculated fracture orientation, fracture dimension and density. Fischer and Guest (2011) note that both tensile and shear failure can be inverted from the seismic moment tensor and reason that shear failure is often accompanied by some tensile component of failing. Goertz-Allmann et al. (2015) have introduced

methods of using the magnitude and distribution of microseismicity to constrain estimates of permeability and connectivity of fractures.

Measurements of fault lengths have shown to follow a power law relationship (Bonnet, et al., 2001). Gillespie (1993) studied many sandstones and noted the many situations where larger faults were surrounded by many smaller faults following a power law distribution. Several studies have estimated the number of faults at a certain length within reservoirs using a power law distribution e.g (Bour & Davy, 1999) (Bonnet, et al., 2001) (Johri, et al., 2015). Marret (1996) highlights the importance of scaling fault size to frequency, thus showing the relative abundance of fractures at a given size. Bonnet et al (2001) highlights the different approaches for characterizing the power law fracture size and fracture dimensions. The three recognized distributions of fracture sizes are frequency, cumulative frequency and frequency density, whereby the power law holds for fracture size distribution if a straight line of sufficient scale range and acceptable error can be drawn on a log plot. A sufficient scale range is reached when many faults of over a range of lengths have been measured, thus achieving a good representation of the number of faults at a certain lengths. Bonnet et al (2001) cites the density distribution as the most applicable method for geologists, therefore this method was adopted.

The spatial distribution of faults is highly irregular in comparison to length scaling as they are controlled by layer thickness and mechanical differences between layers. Thus, many researchers use a random distribution. However, using a random distribution of fractures within the reservoir does not emulate physical relationships as simple field observations indicate that faults are likely to be of a higher density in certain weaker lithologies. Perhaps more importantly for this study is the fact that smaller faults and fractures are likely to be more numerous in the proximity of larger faults. This was found in research conduction on the Barnett shale by Gale et al. (2007) who found fractures present in echelon arrays. Furthermore, it is stated that smaller faults are often concentrated around larger faults and are described as damage zones (Nicol, et al., 1996). Many studies neglect this such as Fang et al (submitted) where a random fault network was assumed or Segall and Lu (2015) where a uniform N-S strike of faults was assumed. There are several ways in which to improve this such as introducing an average distance *d* between the center of a fault with a length l_n and its closest neighbor with a larger length (Bour & Davy, 1999). Bour & Davy (1999) applied this methodology to the San Andreas fault zone and found that using fractal fault spacing emulated nature, such that larger faults were situated further away from each other than smaller faults. They conclude that a scaling law with an exponent around 0.25 is sufficient to describe the distance between faults.

For the most part, production is determined by existing faults and fractures and their distribution within the reservoir (TerHeege, 2016). Gong and Rossem (2014) argue fluids will preferentially travel through certain reactivated fractures in a process referred to as flow channeling, of which is attributed to the broad range of fracture conductivities within the reservoir. This is significant for this study as it suggests that reactivating a population of faults that follow a power law distribution may be a meaningful way of characterizing productivity.

Criteria for a successful shale

Both the Posidonia and Geverik lithologies represent the most prospective shale plays in the Netherlands because of their high total organic matter content (TOC), adequate thickness, thermal maturity and geomechanical properties. As of yet, no gas has been extracted from either lithology,

hence throughout this thesis we compare the Posidonia and Geverik to shale reservoirs currently producing i.e the Barnett, Marcellus and Woodford Shale.

TOC is relevant to this study as it is one of the main factors when estimating the porosity and is related to gas sorption. Most of the gas present in shales resides in the pores within organic material and absorbed into the organic minerals. Many authors, such as Meissner (1978); Schmoker; Hester (1989) and Nixon (1973) state that TOC can be observed in well logs where researchers observe the stark increase in resistivity with increasing TOC. Additionally, sonic log waves reduce as porosity in organic matter is typically higher than in clay rich matter. Passey et al (1999) cites increases in hydrocarbons as the reasoning for this. Economically viable amounts of gas require a certain thickness and Bergen et al (2013) state that a thickness of 30-32m is sufficient.

When applying elementary modelling techniques, the potential for tensile and shear fracturing is controlled by the geomechanical properties of the reservoir. Activation of fractures in shear is controlled by the magnitudes of shear and normal stresses as well as the coefficient of friction. Whilst the ability for rocks to fracture under tension is often referred to as brittleness (Cho & Perez, 2014). Brittleness is related to a rock's cohesive strength, lithology, texture, effective stress, temperature, fluid type, diagenesis and TOC (Wang & Gale, 2009). Effective stress, temperature and diagenesis is heavily controlled by depth. When depth increases so does the temperature, resulting in increased diagenesis and reduced TOC. Wells (2004) reasons that chemical alteration results in silica enrichment arises due to diageneses where there is a transition of smectite to illite. For this study, we define the brittleness with the magnitude of Youngs modulus and Poisson ratio and assess how they influence the geometry of tensile fractures. King (2010) cities the increase in silica and detrital calcite whilst Grieser et al (2007) reasons that this change in mineralogy results in a high Young's modulus and low Poisson ratio i.e a good brittleness index. For example, analysis of the Barnett Woodford Shale in the Delaware basin and the Barnett-Shale in the Fort Willian Basin concludes that the higher temperature and effective stresses present in the Barnett-Woodford shale increases its ductility and fracture strength, reducing the effectiveness of stimulation (Wang & Gale, 2009).

Study areas

Posidonia

The Posidonia shale formation features prominently throughout Northwestern Europe, stretching from the UK to Germany with thicknesses ranging from 30-60m (Van Bergen, et al., 2013). It consists of dark grey to dark brown bituminous fissile claystones, of which are thought to be deposited during high sea levels with limited sea floor circulation. Van Bergen et al., (2013) calculated the TOC for the Posidonia Shale formation and found a TOC of 5-7%, up to 14% in some areas and predominantly composed of kerogen type II. In the Netherlands the Posidonia Shale Formation is restricted to basin centers which formed in the Jurassic. Namely the West Netherlands Basin, Central Graben Basin and Saxony Basin and only reaches maturity in deep synclinal geological features (Herber & de Jager, 2010). Wong et al. (2007) argues that deposits are restricted to basin centers because late inversion events led to erosion at basin margins. The well locations used in this study are presented in Figure 2 and were chosen to incorporate a solid spatial distribution of the Posidonia Shale.

Geverik

The Geverik Member was deposited during the Namurian and for this study we use EMO-01 and GVK-01 (Figure 1) as they contain the required data. The Geverik makes up part of the lower Epen formation and has a maximum thickness of 50m, composed of bitumous black which has been slightly silicified and calcareous. It's bitumous composition and high TOC of around 9% means that shale gas recovery is a potential in the Geverik Shale. Zijp et al. (2015) studied 66 core samples observing dark shales with a number of faults and fractures, often filled by calcites. The shales were composed mainly of type II kerogen with a TOC ranging from 2-9%, average porosity of 11%.

Figure 2 Map showing the locations of the wells used in this study. Wells EMO-01 and GVK-01 were used to assess location specific reservoir properties in the Geverik, whilst the remainder of wells assessed the Posidonia.

Modelling approaches

Hydraulic fracturing simulator

MFrac is a pseudo 3D hydraulic fracturing simulator that incorporates coupled parameters impacting fracture propagation and proppant transport (Mayer & Associates , 2011). The fully coupled heat transfer and proppant transfer routines allow the user to program treatment schedules and fracture design (Mayer & Associates , 2011). Crucially, MFrac assumes an initial homogenous unfractured reservoir, in which to simulate the tensile opening of fractures (mode I fractures).

MFrac was used to model tensile fractures at each well location and required the following inputs; Young's modulus, Poisson ratio, in situ stress conditions, permeability, fracture toughness, spurt loss and fluid leak-off data. These variables were calculated using petrophysical analysis of sonic (*DT*),

bulk density (RHOB) and resistivity (RHOB). Fracture toughness was set at 2000 and spurt loss 0 following Ter Heege (2016).

Dynamic Young's modulus & Poisson ratio

Preferably compressional (V_p) and shear wave (V_s) velocities were calculated form dipole sonic logs. In some circumstances (V_s) velocities were calculated using an empirical relation (Equation 1) (TerHeege, 2016).

Equation 1

$$V_s = \frac{V_p - 1.16}{1.36}$$

Once compressional and shear wave velocities were calculated dynamic Young's modulus (*E*) and Poisson ratio (*v*) calculated using Equation 2 & Equation 3:

Equation 2

$$E_{dyn} = \rho b \, V_s^2 \frac{3V_p^2 - 4V_s^2}{V_p^2 - V_s^2}$$

Equation 3

$$v_{dyn} = \frac{V_p^2 - 2V_s^2}{2(V_p^2 - V_s^2)}$$

Although this method provides an estimate of the *E* and *v* of the reservoir we suggest that static methods are more valid. Eissa and Kazi (1988) cite the superiority of static methods for assessing Young's modulus when compared to dynamic methods. Furthermore, there is a poor correlation between static and dynamic Young's moduli with static estimates generally lower than dynamic estimates (Ter Heege, et al., 2015). Static measurements are conducted on rocks under recreated reservoir conditions making them more reliable. This method is relatively time consuming and expensive, thus dynamic methods were more applicable.

In situ stress

MFrac requires the overburden stress (*Sv*) and the minimum horizontal stress Sh_{min}, the latter calculated by MFrac using Eatons method. *Sv* is determined using gravitational acceleration (g), bulk density (ρ) and depth (z) with Equation 4:

Equation 4

$$Sv = \int_0^z \rho(\mathrm{z}).\mathrm{g}.(\mathrm{z}).\mathrm{dz}$$

The minimum horizontal stress is calculated using Eaton's method which assumes that the reservoir is laterally constrained and that horizontal stress is controlled by the overburden weight (Fox et al., 2013). The equation draws on *Sv,* Poisson ratio (v) and pore pressure (*Pp*) through Equation 5:

Equation 5

$$S_{hmin} = \left(\frac{v}{1-v}\right)(S_v - P_p) + P_p$$

Permeability and leak off

The most renowned technique for assessing permeability is the coring sections of lithology and testing its permeability when subjected to similar reservoir conditions. This practice is expensive and time consuming, thus many researchers have attempted to assess permeability through empirical methods. For this study permeability was empirically related to total porosity through the following method. As previously stated porosity is largely controlled by the organic content of the shale, therefore we relate the relative abundance of TOC to the matrix.

The method of identifying areas with high TOC is as follows; firstly, resistivity and sonic logs are scaled so that their base lines overlap in organic poor water saturated intervals (*RESD_BASE & DT_BASE).* Secondly the curve separation (*ΔlogR)* is calculated with Equation 6:

Equation 6

$$\Delta logR = log_{10}\left(\frac{RES}{RESD_{BASE}}\right) + 0.02 * (DT - DT_{BASE})$$

Finally, *TOC_LD* is measured in areas which are organic rich with **Equation 7** where LOM denotes the level of organic maturity:

Equation 7

$$TOC_{LD} = \Delta logR * 10^{(2.297 - 0.1688 * LOM)}$$

The porosity was determined using *TOC* and bulk density taken from the bulk density log *(RHOB)* Equation 8*.* Furthermore, maximum and minimum porosities were defined by maximum and minimum densities taken from the RHOB. The following constants were assumed in this study an average density; of the matrix ($\rho_{mat} = 2.7(g/cm^3)$), pore fluid ($\rho_f = 1.05(g/cm^3)$ and gas ($\rho_g = 0.2(g/cm^3)$). Water saturation is difficult to define because the different methods of calculating saturation often yield different results. We use an average ($S_w = 0.5$) based on relevant data from US shales (TerHeege, 2016).

Equation 8

$$Porosity\ \phi = \frac{\rho - \rho_{mat} + TOC.\rho_{mat} - \rho.TOC^{TOC}}{TOC.\rho_{mat} - \rho_{mat} - \rho.TOC^{TOC} + S_w.\rho_f + (1 - S_w).\rho_g}$$

Permeability was calculated by means calculating maximum and minimum porosities and empirically relating this to maximum and arithmetic mean permeability through Equation 9. This method results in the relational type:

Equation 9

$$k = C_1 . e^{c_2 \phi}$$

Where k is in ND and C_1 & C_2 yielded 39.9 & 33.6 respectively, with values taken from (TerHeege, 2016). This method has limited validity and must be treated as a rough estimate because it is a simple empirical relation based on plotting maximum and minimum porosity against maximum and minimum permeability.

The leak off coefficient L_c has a profound effect of fracture dimensions and the most robust method for assessing this is through extended leak off tests. However, in the absence of well tests a relation was used based on the Marcellus shale where $L_c = 0.5k^{0.55}$. A maximum and minimum case was defined by firstly the corresponding permeability, then later L_c*0.2 and $L_c * 5$ since the former maximum and minimum L_c did not account from the variations reported for other tight reservoirs (TerHeege, 2016).

Equations for assessment of fracture volume relationships

2D models are useful when assessing the effects of parameters on fracture propagation. This study uses the Perkins-Kern-Nordgren (PKN) and Khristianovic-Geertsma-de Klerk (KGD) (Equation **10** & Equation 11) taken from (Economides & Boney, 2000). Both equations explore the relationship between length (L) and width (w), whilst assuming a constant fracture height (h). In this way one can vary the Pe (Pressure-Sh_{min}), Poisson ratio and Young's modulus and analyse their impact on widths and height. The PKN equation is used when Length is much greater than height and the KGD when the height is much greater than length. Nasirisavadkouhi (2015) suggests that the relationship between height and length is controlled by the vertical variation of Sh_{min}. When Sh_{min} is greater in the reservoir than confining layers, height will be much greater than length (Nasirisavadkouhi, 2015). This situation often exists where lower density sandstones confines a shale layer.

Equation 10

PKN $w = \frac{\mathbf{4(1-\nu^2)LP_e}}{\mathbf{E}}$ where $P_e = Fracture\ pressure = Pp - Sh_{min}$

Equation 11

KGD $w = \frac{\boldsymbol{\pi(1-\nu^2)LP_e}}{\mathbf{E}}$

Appendix 2 indicates that changes in width have little impact on the overall lengths whereas changes in heights have large impacts on the lengths. Therefore,

Equation **12** was used to analyse the relationship between height and length whilst assuming a constant width. The equation creates fractures in terms of pump rate q_i , pumping time t_p, fluid loss c_l, fracture height and width h_l & w, spurt loss S_p and fluid loss height h_f (Economides & Boney, 2000).

Equation 12

$$L = \frac{q_i t_p}{6c_l h_l \sqrt{4h_l + 2wh_f}}$$

Semi analytical natural fracture model

As previously stated modelling approaches which assume no natural fracture network have some limitations, especially when characterizing permeability. This study uses a power law distribution to characterize natural fractures in a reservoir and assess the potential to predict fluid flow. Essentially, we present a reverse modelling approach in which we distribute fractures and induce failure by increasing the pressure in the whole reservoir uniformly. We then use the reactivated fractures to create an ellipsoid representing the stimulated reservoir volume (SRV). We update the permeability and model fluid flow within the ellipsoid and compare the fluid volume required for failure with the total cumulative seismic moment.

Synthetic Fault network

To introduce natural fractures into a fractured reservoir a synthetic fault network was developed with a size range following a power lar distribution and a weighted probability regarding their distribution in space.

Fault lengths

It is necessary to explain some of the discourse used when considering power law distributions. Fractal geometry of a fault system uses fractals, which are repeated patterns of a certain scale referred to as self-similar patterns (Bonnet, et al., 2001). Fractals are unique to other geometric features when considering their scaling characteristics. For example, by doubling the radius of a sphere the volume of the sphere increases by a factor of 8 because the radius doubles and the sphere increases by a factor of 3. When a one-dimensional length is doubled then the increase may not be an integer but a fractal dimension. The power law describing distribution is given in Equation 13 (Bonnet, et al., 2001). Where $N(l)$ is the number of lengths which occur in the interval $l, l + dl$, of which is described by the scaling factor α of length l and *a* is the exponent of l (Bonnet, et al., 2001). If the bin size is constant then α and *a* are equal, if the bin size progresses logarithmically then the exponent becomes $\alpha - 1$. The density distribution *N(l)* is the number of lengths within an interval divided by the bin size, thus smaller fractures will be more numerous and therefore have a higher frequency Figure 3. One must select an appropriate bin to avoid fluctuations in frequency's when plotting. Bonnet et al (2001) reasons that the choice of the interval dl is important regarding the smoothness of the data.

Equation 13

$$N(l) = \alpha l^{-a}$$

N=number of faults

l=length of fault

α=scaling factor related to the minimum fault length

a=exponent between 1 - 3

The log-log plot of fault lengths gives a straight line and the gradient of the straight line gives the exponent value.

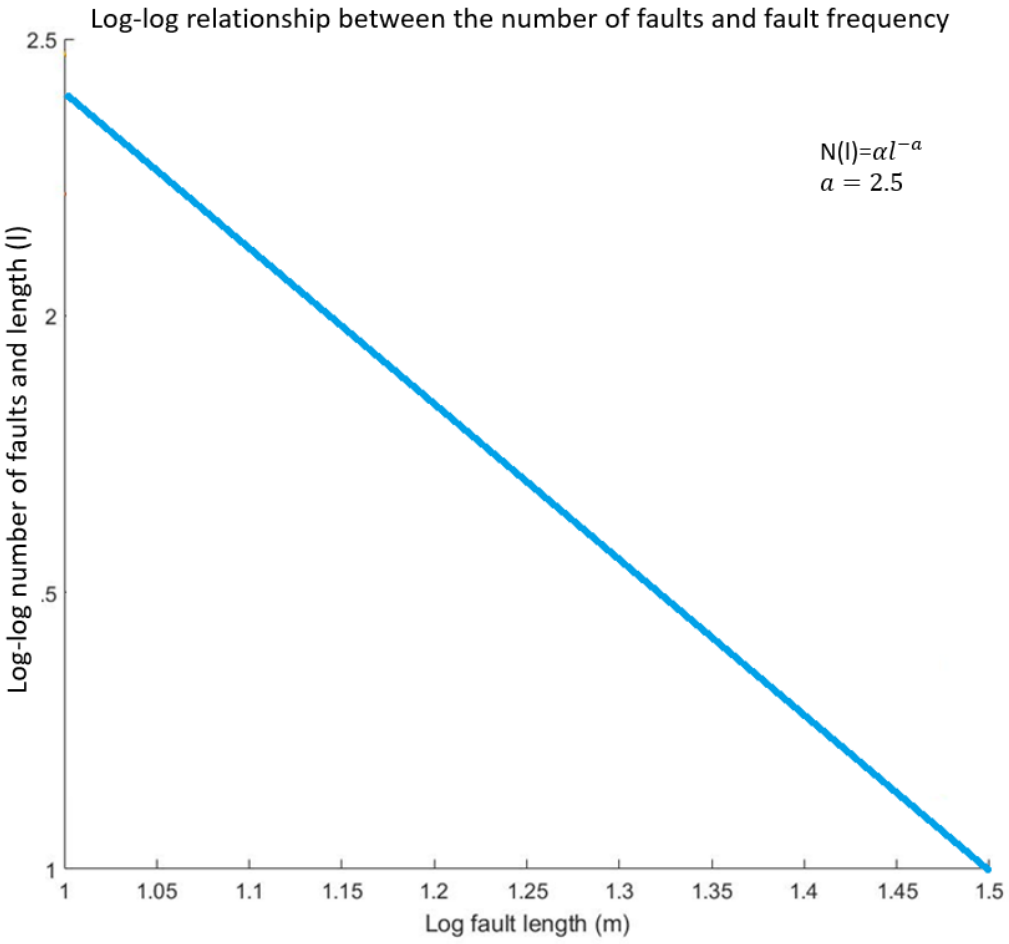

Figure 3. plot shows the log-log power law relationship inferring the frequency length distribution

Fault distribution

Initially all faults were randomly distributed throughout the reservoir resulting in Figure 4a. As previously stated, this is not what is observed in nature, hence faults were distributed with a weighted probability. Faults are sub divided into large, medium and small faults to simplify the way in which they are distributed spatially. In nature, it is documented that large faults are situated apart from each other, therefore latin hypercube sampling *(LHS)* is used to ensure that the center of large and medium sized faults aren't situated next to each other. LHS enables the model to "remember" the location of the fault centers and can be thought of as Monte Carlo sampling with memory. LHS solves the problem of locating faults next to each other by ensuring a significant distance between fault centers. To increase the chances of smaller faults being placed next to larger faults circles are drawn around each fault and smaller faults were given a 50% chance of being randomly placed at a location in the circles surrounding large faults, a 25% chance of being randomly placed at a location in the circle surrounding medium faults, and a 25% chance of being randomly distributed within the reservoir. Figure 4 a&b compares faults which are randomly distributed (Figure 4a) to those distributed with a weighted probability (Figure 4b), developed in this study. Figure 4b clearly shows

the higher concentration of smaller faults surrounding larger faults. This approach improves the characterization of the distribution of faults as it better represents the observations made at outcrops. Furthermore, this method advances the approaches of other studies such as Fang et al (submitted) and Seagal and Lu (2015) where a random distribution is used.

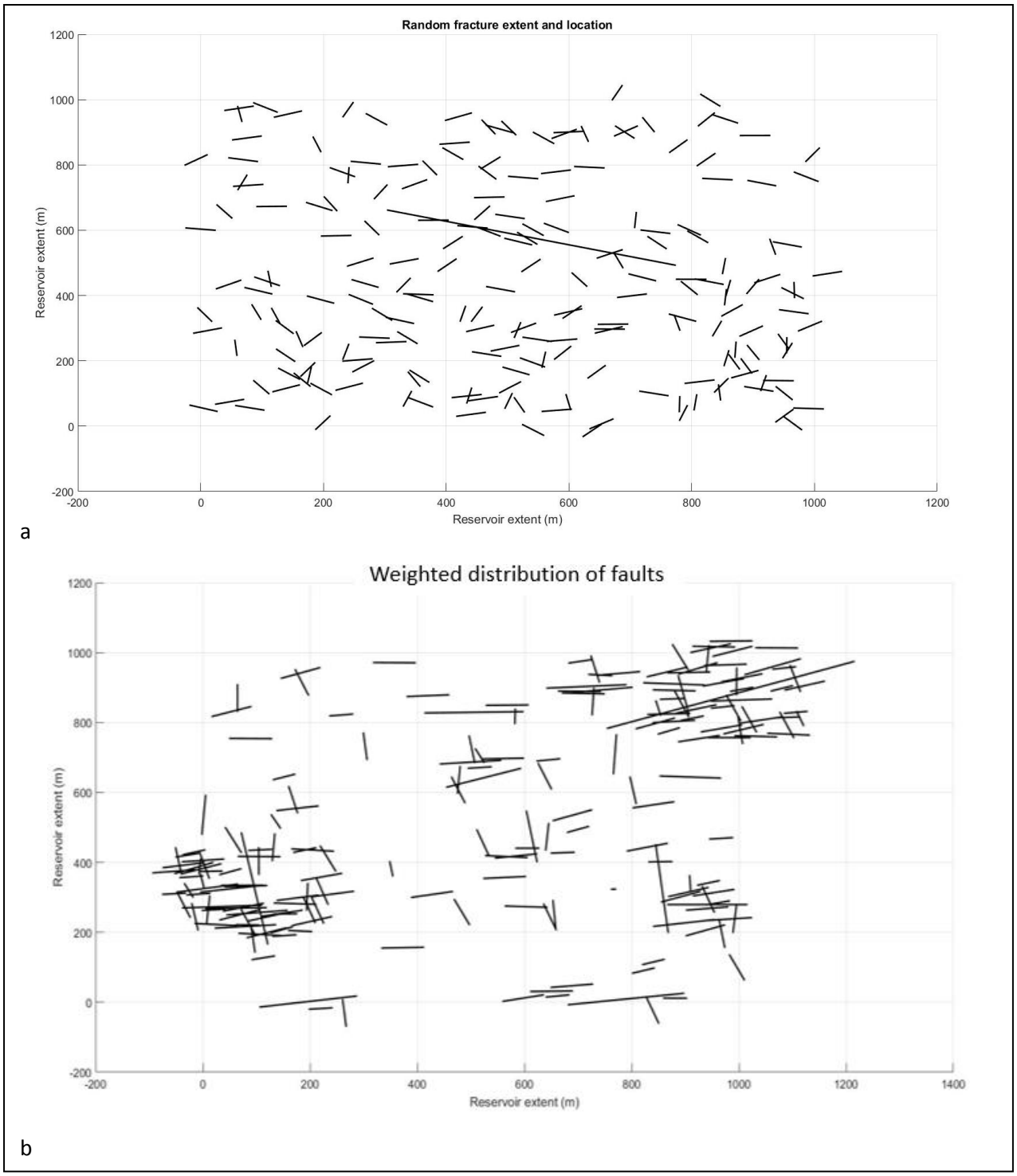

Figure 4 Randomly located faults in 2D following Monte Carlo random distribution. Figure 4b Weighted probability distributed of faults developed in this study. It is important to notice the clustering of faults in Figure 4b where small faults are located around larger faults. The representations of faults in this manner will impact permeability maps.

Displacement on a fault plane and seismic moment calculation

Seismic moment magnitudes are dependent on shear strength, fault length and the rupture area on each fault. Displacement is defined as the total distance between two points which were originally adjacent prior to a seismic event (Kim & Sanderson, 2005). The complexity of fault displacement is highlighted by Schlische, et al (1996) who reason that displacement is greatest in the fault center and dissipates to zero at the fracture tips. This can be visualized in Figure 5 where displacement is greatest at the midpoint of the fault length (A-B).

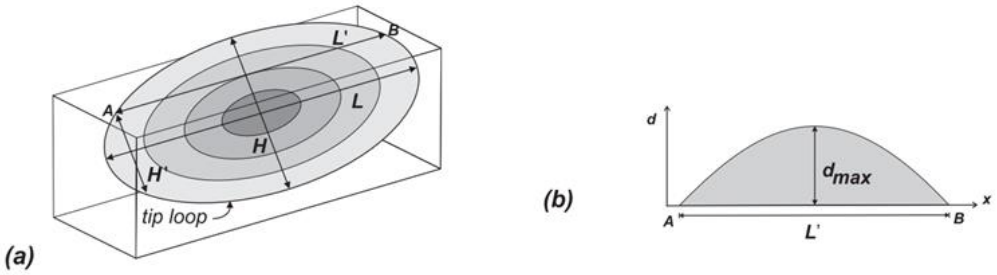

Figure 5a Image shows a fault plane modelled as an ellipsoid. Figure 5b shows displacement differences with strike length. H refers to the height of the fracture, L the length measured at the cross section of A and B.

Research conducted by Schlische et al (1996) found no difference between fault size and the distribution of displacement along the fault plane, implying that the displacement style as discussed earlier may be consistent for fault planes of different sizes. The factors controlling the maximum displacement and fault length are summarized as; the material properties, the faulting regime including its position and direction of movement, earthquake and slip propagation history, reactivation and segmentation and linkage. The material properties are the type of lithology or more importantly the lithology change and relates to the concept of small and large faults. Small faults are classified as those which are contained within a single layer whilst larger faults propagate through several layers. Faulting regimes influence the ratio of length to maximum displacement as follows; strike slip faults have a higher ratio than dip slip faults and normal faults (Kim & Sanderson, 2005).

The average displacement d is related to the maximum displacement, which is in turn a function of stress drop and fracture stiffness Equation 14. The average d is related to the maximum d_{max} through Equation 14. d_{max} is described by Brune (1970) the largest displacement following 100% of stress drop which is governed by Equation 14.

Equation 14

$$d = \frac{2}{3} * d_{max} = \frac{2}{3} * \frac{\Delta\tau}{k_s}$$

$\Delta\tau$=stress drop

k_s=fracture stiffness

The stress drop calculated in Equation 15 was assumed to be constant across the entire fault plane.

Equation 15

$$\Delta\tau = \Delta\mu_{ss} * \sigma_n'$$

$\Delta\tau$=stress drop (Mpa)

σ_n'=effective normal stress (Mpa)

$\Delta\mu_{ss}$=change in friction coefficient

k_s denotes the fracture stiffness and is one of the most important parameters to define, as rock deformation will preferentially occur in fractures and the stiffness controls at what stress failure will occur (Jiang, et al., 2009). k_s is defined as the rate of change in normal stress with respect to fracture closure and assuming penny like fractures resulting in Equation 16

Equation 16

$$k_s = \frac{G*\eta}{l}$$

l=fracture radius (m)

η=geometric factor (rad)

G=shear modulus (GPa)

The geometric factor η was taken from Dieterich (1992) with a value of 7π/24 and l is the radius of the fracture (Fang et al., submitted). The seismic moment (M_o) is calculated with the shear modulus (*G)*, displacement (*d)* and area (*A*) on a fault Equation 17 (Wassing, et al., 2014). Length of the fault was estimated using a power law relation and the width if the fault was assumed to be half its length.

Equation 17

$$M_0 = G.d.A$$

Moments can vary considerably therefore moments are often presented in terms of moment magnitudes (M_W) which is a logarithmic relation Equation 18:

Equation 18

$$M_w = \frac{2}{3} * logM_0 - 10.7$$

Traditional measurements of earthquake magnitudes use the Gutenburg-Richter (G-R) relation, which expresses the number of earthquakes with a certain magnitude. G-R relation is a natural power law distribution which has also been applied to microearthquakes resulting from hydraulic fracturing (Eaton, et al., 2014) (Grob and van der Baan, 2011) Equation 19. The relation is introduced by (Davies, et al., 2013) as where a, b and M are parameters describing the seismicity of the region, the slope of the frequency magnitude plot and the maximum earthquake size (Osinga, et al., 2015):

Equation 19

$$logN = a - bM$$

Where a, b and M are parameters describing the seismicity of the region, the slope of the frequency magnitude plot and the maximum earthquake size (Osinga, et al., 2015). Higher a and b values reflect elevated levels of seismicity with a high number of small events. This method is an empirical relation measuring the characteristics of the seismogram and not the actual source energy (Davies, et al., 2013).

Cumulative seismic moment

McGarr (1976) proposes that in other situations describing seismicity in terms of volume change is more intuitive, especially when considering fluid injection. This study concerns earthquakes generated from the injection into a low permeability reservoir and a simplistic approach would be to relate the volume of injected fluids to the volume of deformation. If one considers a cube representative of reservoir rock under a constant stress applied by the principal stresses σ_1, σ_2 & σ_3. Inducing a volume change$(\Delta \mathrm{V})$ from the injection of a fluid will alter the principal stresses and strains acting on the cube. McGarr (1976) stresses the importance of the assumption that readjustments of the stress field to a new equilibrium are only possible through seismic failure. The volume change is accommodated by a strain change in the same direction and the associated stress drop (Randall, 1971). For the linkage of stress drops to the total seismic moment, earthquakes are treated as failure events throughout the volume. In this way the total seismic moment is related to the change in shear stresses and volume (McGarr, 2014) Equation 20. Essentially, this method assumes that all the fluid injected results in seismicity under the assumption that all faults are critically stressed. Therefore, it can be used to predict the maximum possible cumulative seismic moment.

The total seismic moment can be treated as a scalar measurement of seismic deformation which describes the moment in terms of volume change ΔV, shear modulus G and *K,* factor ranging from 0.5 to 1, Equation 20a (McGarr, 1976). Following McGarr (2014) a second relation for cumulative seismic moment can be derived from Equation 20b, which differs by around a factor of 2. The differences in both equations stem the fact that in Equation 20a, McGarr (1976) assumes that volume change impacts the deviatoric stress, which is relaxed during an earthquake. In this way seismicity counterbalance the increase in shear stress resulting from a change in volume. Equation 20b assumes that each fault is roughly half a seismic stress drop below the maximum stress required for failure. Therefore, McGarr (2014) assumes that it takes around half as much fluid induced stress change to induce slip, explaining the larger magnitudes estimated by Equation 20b. For this study we adopt Equation 20b as it is designed for fluid induced seismicity, whereas Equation 20a was formulated using actual rock volume changes.

Equation 20

$$\sum M_0 = KG\Delta V \text{ (a)}$$

$$\sum M_0 = 2G\Delta V \text{ (b)}$$

Fluid volume required for failure

The following introduces a short summary of the steps taken to calculate the fluid volume required for failure:

1. Pore pressure was uniformly increased throughout the entire reservoir, from this number of faults failing and their respective moment magnitudes are calculated.
2. We then calculate permeability within an elliptical stimulated reservoir volume. A pseudo injector well is 'placed' in the centre of the reservoir and the furthest reactivated faults away from the central point is measured.
3. The distance of the outermost reactivated faults away from the centre define the radii of the ellipsoid and the yield pressures at the edge.
4. We then inject fluid at a constant flow rate and record the time taken to increase the pore pressure enough to induce failure at the edge of the ellipsoid.
5. Flow rate was expressed as volume over time to gain an estimate of fluid volume.

This way we validate the model by linking the cumulative seismic moment based on fluid volumes to the cumulative seismic moments calculated in the model.

Estimating fluid rates required a robust characterization of permeability. Permeability was represented as 3D tensors, where each tensor was transformed according to the orientation and dip of individual fractures, in relation to the coordinate system of the model. For simplicity, the dominant permeability direction was assumed to be parallel to the y axis of the reservoir.

Fracture aperture

Fracture opening, both in normal and shear directions controls the permeability. The former results from pore fluids forcing the fracture to open perpendicular to the fault plane. The latter forms when two asperities on either side of the fault plane slide past each other resulting in opening (Fatehi Marji, et al., 2011) . Furthermore, Fatehi-Marji, et al. (2011) reason that shear dilation accounts for much more of the total fracture volume than tensile opening of fractures. Fang et al. (submitted) relates the shear aperture b_s to the displacement (d) and the dilation angle (ψ_{dil}) Equation 21. Rosqvist et al. (2008) specify that normal fracture apertures (b_n) are controlled by the normal stresses through Equation 22.

Equation 21

$$b_s = d\ tan\psi_{dil}$$

Equation 22.

$$b_n = b_r + b_{max}\exp(\propto \sigma_n)$$

Where b is the overall fracture aperture, b_r denotes residual aperture b_{max} describes the max aperture when the normal stress (σ_n) is zero and $\propto$ describes the rate of change in aperture with respect to normal stress (Rutqvist, et al., 2008). The total aperture (b) was calculated by summing shear and normal apertures.

Permeability

For individual fractures permeability $(k_{ff})$was described in terms of total aperture *(b)* (Equation 23) (Wassing, et al., 2014).

Equation 23

$$k_{ff} = \frac{b^2}{12}$$

To fully represent fractures within an anisotropic reservoir we decompose fracture permeability into a 3D tensor Equation 24. For this study anisotropic x',y',z' coordinates of a 3D permeability tensor is represented as $[k']_{3x3}$. We assume that the y axis of the model represents the principal direction of permeability, hence the angle of transformation is between the strike (β) and dip (α) of the fault and the y axis of the model (Lei, et al., 2015).

Equation 24

$$[k'] = \begin{bmatrix} cos^2\alpha cos^2\beta k_{ff} & -\frac{k_{ff}cos^2\alpha sin2\beta}{2} & \frac{sin2\alpha cos\beta k_{ff}}{2} \\ --\frac{k_{ff}cos^2\alpha sin2\beta}{2} & cos^2\alpha sin^2 2\beta k_{ff} & -\frac{sin2\alpha sin\beta k_{ff}}{2} \\ \frac{sin2\alpha sin\beta}{2} & \frac{-sin2\alpha sin\beta k_{ff}}{2} & sin^2\alpha k_{ff} \end{bmatrix}$$

For every i^{th} fracture the permeability tensor becomes:

$$ki = \begin{bmatrix} ki_{xx} & k_{ixy} & ki_{xz} \\ ki_{yx} & k_{iyy} & ki_{zy} \\ ki_{zx} & ki_{zy} & ki_{zz} \end{bmatrix}$$

To characterise reservoir permeability future studies should consider an approach which fully incorporates individual fractures. Due to time constraints, we took the following, simplified approach. We construct an ellipsoid representing the stimulated reservoir volume (SRV), characterised in Figure 6, which shows the furthest reactivated faults (coloured circles) from the centre in x,y,z directions. In order to achieve this we constructed a pseudo cross section (coloured lines) in x,y,z and picked the nearest reactivated faults to each end of the cross sections. The distance from the fault to the centre in x,y,z directions were used as radii for the ellipsoid. The SRV was then used to construct an average permeability tensor using both weighted (*w* denotes weighting) fracture $[k_w']_{3x3}$ and matrix $[k_{mw}]_{3x3}$ permeability, representative of the entire SRV. The relative contribution of fracture and matrix permeability were weighted based on their cumulative volume, relative to the volume of the ellipsoid. From this we have an estimation of the bulk permeability in 3D for an ellipsoid in which to calculate fluid flow Equation 25.

Equation 25

$$Weighted\ k = [k_{fw}{}']_{3x3} + [k_{mw}]_{3x3} = \begin{bmatrix} k_{xxw} & k_{xyw} & k_{xzw} \\ k_{yxw} & k_{yyw} & k_{zyw} \\ k_{zxw} & k_{zyw} & k_{zzw} \end{bmatrix} + \begin{bmatrix} k_{mw} & 0 & 0 \\ 0 & k_{mw} & 0 \\ 0 & 0 & k_{mw} \end{bmatrix}$$

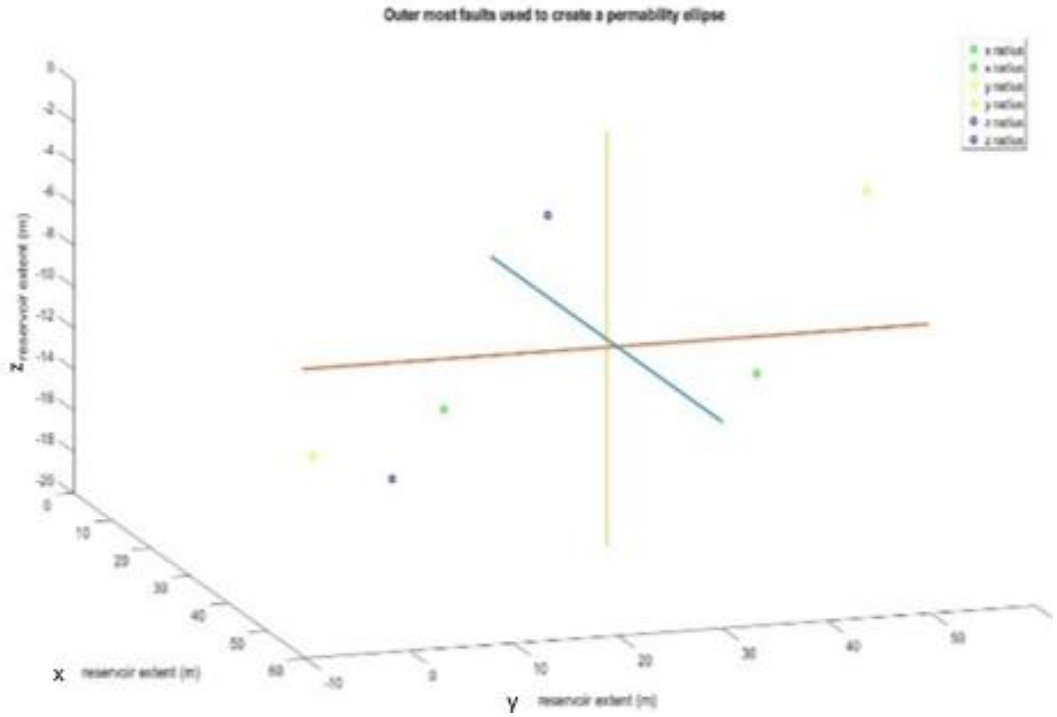

Figure 6 Shows the faults (coloured circles) located closest to end points of a cross section (coloured lines). The distance between reactivated faults were used as the diameter for an ellipsoid representative of a stimulated reservoir volume.

Fluid volume

To calculate the total fluid volume needed to induce failure it was necessary to estimate the fluid volume needed to increase the pressure enough for failure at the edge of the stimulated reservoir volume. Initially the pressure was increased within the whole reservoir leading to failure on faults orientated perpendicular to the minimum horizontal stress. The pressure required to induce failure was calculated using Mohr Coulomb failure, thus the pressure required for failure on the faults characterising the axis of the SRV ellipsoid was known Figure 6.

The permeability tensor was then used to estimate flow rate per unit area in 3D where, [Φ=$p_p - \gamma(\Delta z)$], p_p denotes reservoir pore pressure, $\gamma(\Delta z)$ the hydrostatic gradient and μ fluid viscosity, and A area (m^2) (Franchi, 2008) (Equation 26).

Equation 26

$$q_x = \frac{A}{\mu}[k_{xxw}\ \frac{\delta\Phi}{\delta x} \quad + \quad k_{xyw}\ \frac{\delta\Phi}{\delta y} \quad + \quad k_{xzw}\ \frac{\delta\Phi}{\delta z}]$$

$$q_y = \frac{A}{\mu}[k_{xxw}\ \frac{\delta\Phi}{\delta x} \quad + \quad k_{xyw}\ \frac{\delta\Phi}{\delta y} \quad + \quad k_{xzw}\ \frac{\delta\Phi}{\delta z}]$$

$$q_z = \frac{A}{\mu}[k_{xxw}\ \frac{\delta\Phi}{\delta x} \quad + \quad k_{xyw}\ \frac{\delta\Phi}{\delta y} \quad + \quad k_{xzw}\ \frac{\delta\Phi}{\delta z}]$$

Subsequently, the pumping time required to induce failure on the outermost faults was estimated using Equation 27. We assume a constant flow rate (q) defined by Equation 26 with weighted permeability**,** radius r, initial pore pressure ρ_0, fluid compressibility c and time t (Segall & Lu, 2015). It is important to highlight that this equation describes pressure change in a poroelastic reservoir. The contribution of poroelasticity to the reservoir was not modelled due to time constraints but should be considered for future work Equation 27. Despite of this permeability was low and therefore had a small impact on pressure changes with time.

We increased the pressure in the reservoir until the pressure required for failure at the outer edge of the ellipsoid is reached and the time taken recorded. By solving flow rate in terms of fluid volume and time it is possible to estimate a total fluid volume. Thus, the sum of the total seismic moment was calculated following the method of McGarr (2014) (Equation 20). Thus, formulating an approach to test the cumulative seismic moments within a stimulated reservoir volume, and since McGarr (2014) calculates a maximum value we anticipate the model will predict lesser moment magnitudes.

Equation 27

$$P(x,t) = \frac{q\,\mu}{\rho_0 rk}\, erfc(\frac{1}{2}\xi)$$

Where:

$$\xi = \frac{r}{\sqrt{ct}}$$

Results of model simulations

Simulations of tensile fractures

In the following the simulated fracture dimensions for several locations within the Posidonia and Geverik are presented. Tensile fractures were calculated with reservoir elasticity, pore pressure, in situ stress, porosity and permeability at each location. Firstly, we present the results from equations 11 & 12., showing how different reservoir conditions at each location impact tensile fracture dimensions. Subsequently, we present the results of fracture lengths using simulations in MFrac in terms of both reservoir properties and operational parameters.

Explanation of trends in fracture dimensions, Equation 11 & Equation 12

The following explains the reasoning for differences in fracture dimmensions at each well in terms of Youngs modulus, Sh_{min} and poisson ratio. To explain differences in width and length the pseudo-3D (P3D) fracture models Perkins-Kern-Nordgren (PKN) (Equation **10**) and Khristianovic-Geertsma-de Klerk (KGD) (Equation 11) were used. Results from both equations were similar but the KGD equation matched the Mfrac results better. This is because higher stresses were frequently calculated within the Posidonia and Geverik compared to confining layers. Resulting in larger fracture heights, and as previously stated this circumstance is best captured by KGD equation. When comparing widths and height the vertical heights of fractures were fixed.

The volume of injected fluid was constant at all sites, therefore the volume of fracture should be fairly similar even after accounting for fluid loss as permeability was largely similar across all locations. I.e a shorter fracture will be accommodated with height. For analyses of this relationship a ratio of length to height was plotted against Poisson ratio, Young's modulus and stress using

Equation **12**. Fluid loss height, fluid viscosity, injection rate and volume were all held constant at each location.

Poisson ratio

The effects of the Poisson ratio, Young's modulus and minimum horizontal stress at each location was analysed by (Equation 11). Initially the analysis was run for width whilst holding a constant length of 40 m, subsequently Equation 11 was rearranged to make length the subject and widths were held constant at 20 mm.

Figure 7 shows that the Poisson ratio has a limited effect on length and width considering that the overall widths vary less than 8 mm and lengths 0.5 m. Figure 8 shows no discernable trend in the ratio of height to length. The reason for this is related to the small variation in the measured Poisson ratios, ranging from 0.24 to 3.2 .

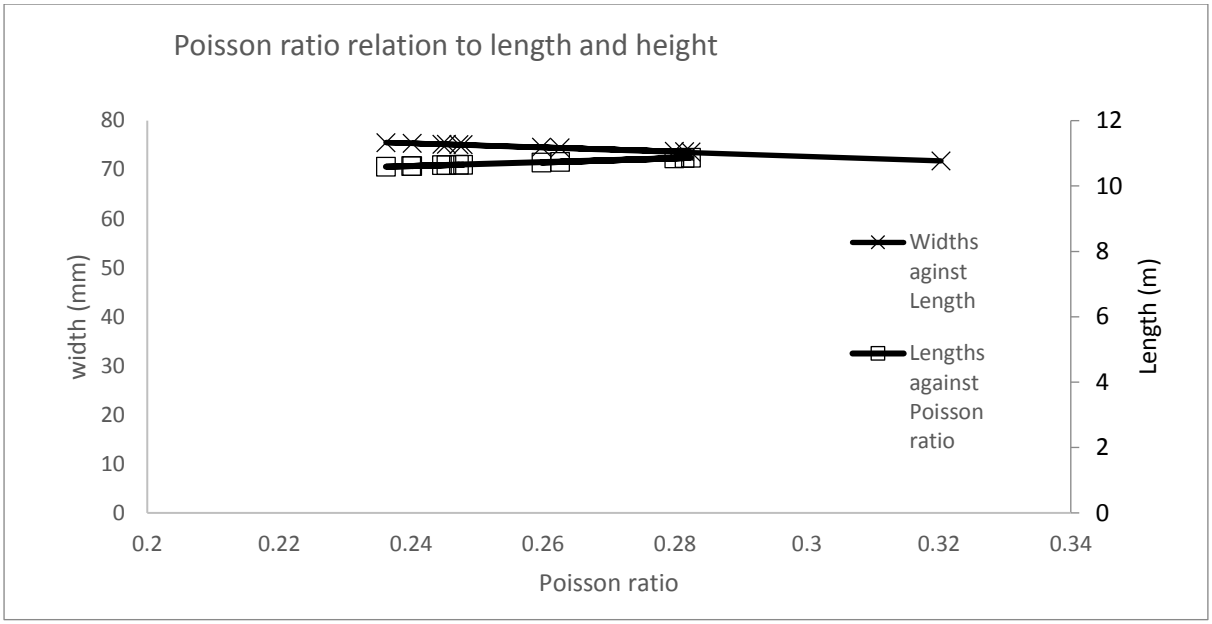

Figure 7 Shows the relationship between Poisson ratio and length (m) & width (mm).

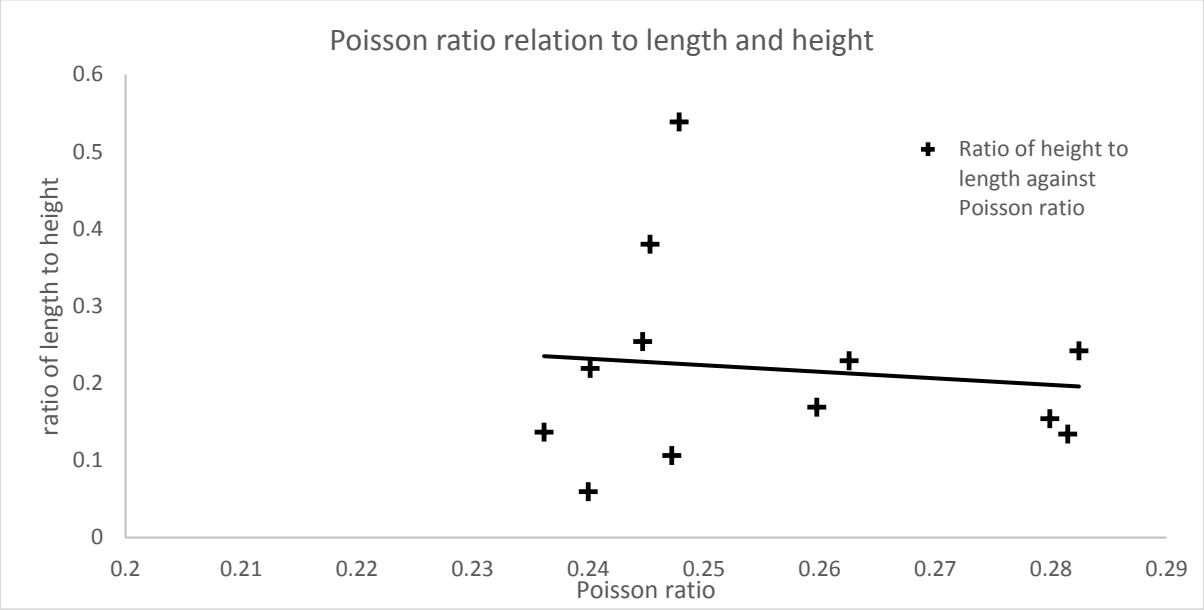

Figure 8 Shows the relationship between Poisson ratio and the ratio of length to height with high ratios indicative of long fractures.

Youngs Modulus E

The impact of the different Young's moduli on fracture width and length is more apparent. There is a clear negative trend between Youngs modulus and fracture width compared to a near linear positive relationship with length (Figure 9). The width of fractures ddecreases with increasing Youngs modulus exponentally . This suggests that either widths are more sensitive to low magnitudes of Youngs modulus where widths rapidly dcrease up util around a youngs modulus of 30 GPa. We also observe a clear trend in increased ratios of length to height with increased Youngs modulus *(*Figure 10).

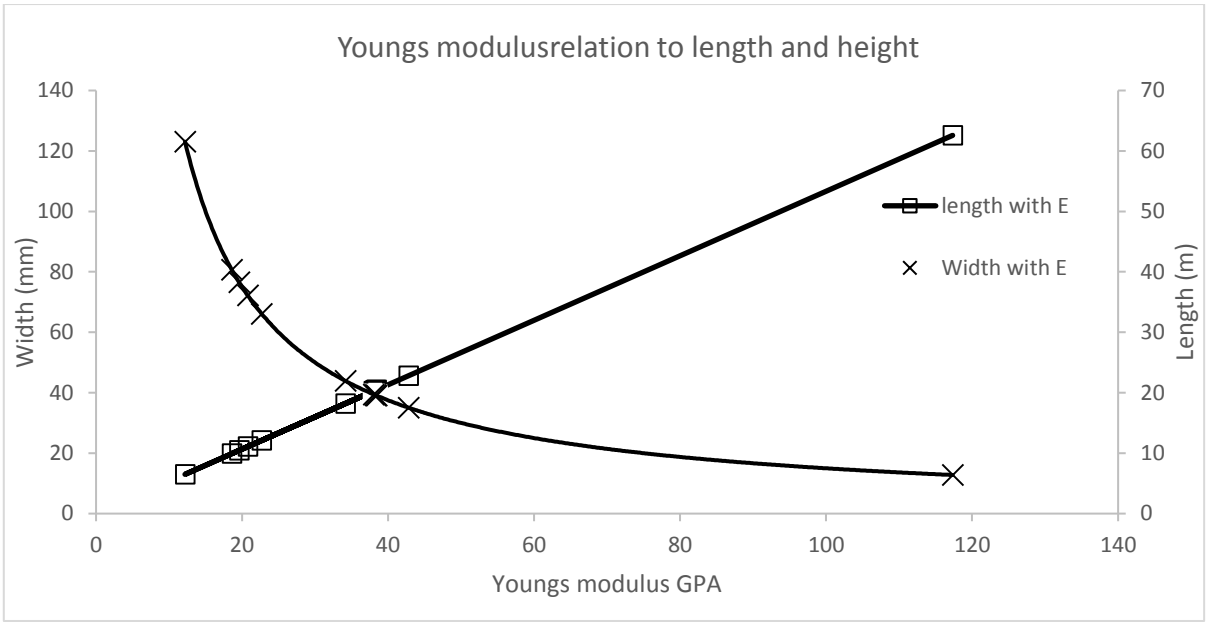

Figure 9 Young's modulus against length and width of fractures. The plot shows a positive correlation between length and Young's modulus and negative for width and Young's modulus.

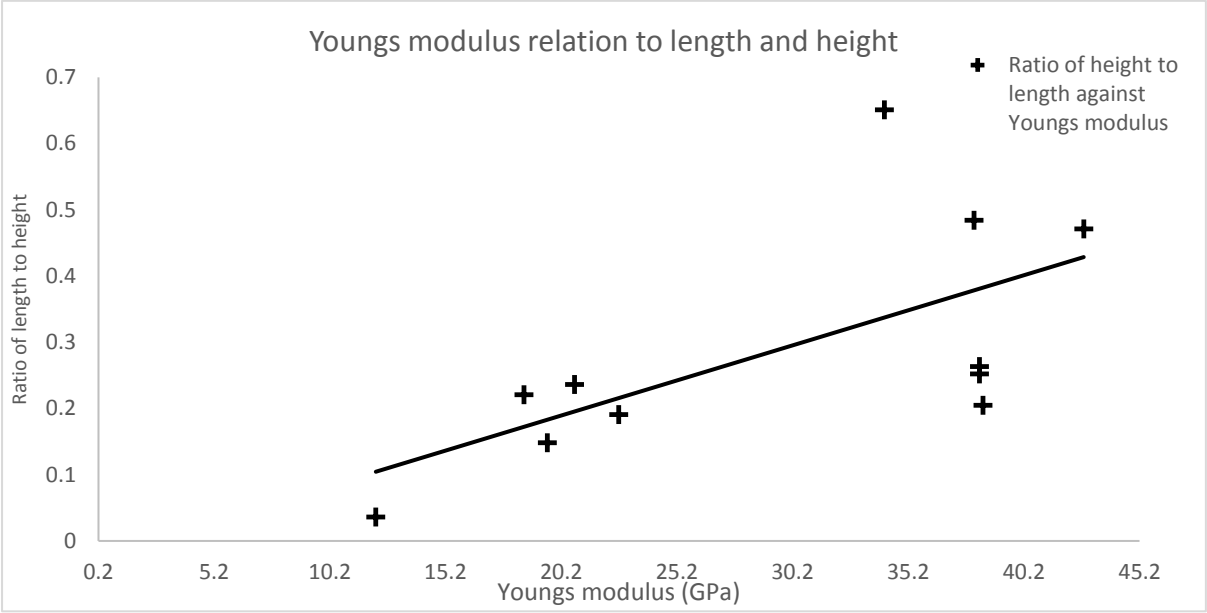

Figure 10. Shows the relationship between Young's modulus and the ratio of length to height with high ratios indicative of long fractures.

Impact of minimum horizontal stress on fracture dimensions

The impact of minimum horizontal stress on fracture dimensions was tested by allowing the Sv and Pp to vary with depth whilst holding injected fluid pressure constant over all wells, since stresses are related to fracture pressure (KGD equation). Sh_{min} is calculated from Pp, Sv and v following Eaton (1969), therefore v was held constant at 0.3. There is a negative trend between fracture width and Sh_{min}, meaning that at lower Sh_{min} magnitudes, fractures will wider. Tensile fractures propagate perpendicular to Sh_{min}, therefore with lower Sh_{min} magnitudes stresses opposing horizontal opening will be less. The opposite trend is found for length, where lengths increase with increasing

Sh_{min}. Additionally, a constant width of 20 (mm) was assumed when modelling the relationship between height and length. The results show increases in the ratio of length to height with increasing Sh_{min}.

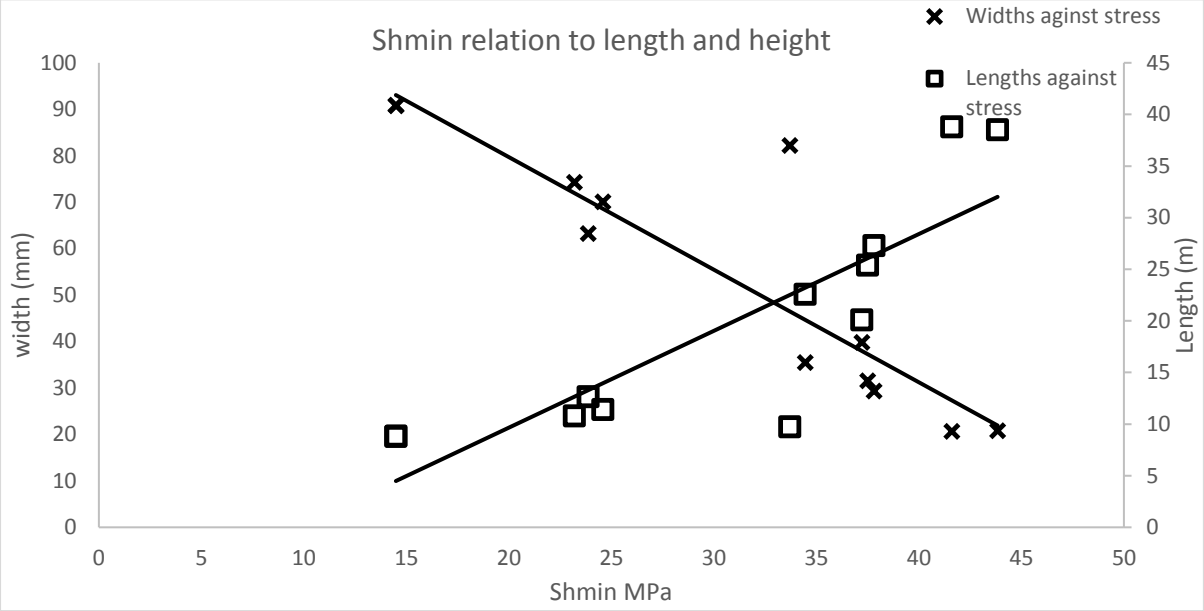

Figure 11. Shows the contrast between height and width with differing magnitudes of stress

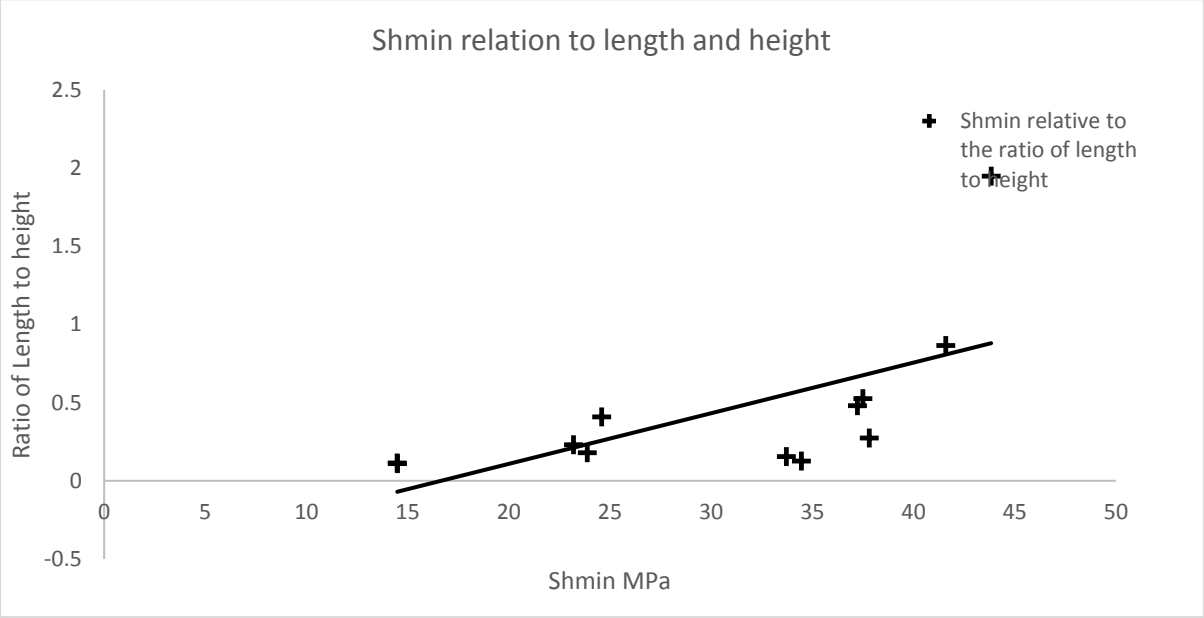

Figure 12. Shows the relationship between Sh_{min} and the ratio of length to height with high ratios indicative of long fractures.

MFrac fracture simulations

Operational parameters

The operational parameters were constant across every well in the study area. Appendix 1 shows that reducing both the rate of fluid injection and the volume separately yielded smaller fractures. In

these situations the ratio of fluid loss to fluid being replaced is lower than the base case scenario, leading to a smaller build up of pressure and reduced fracture propagation. The use of 0.2Lc and 5Lc had the largest influence on fracture size. According to Economides& Boney (2000) fluid loss is always greatest at the tip, explaining the lesser fracture lengths when a high leak off was selected. The higher leak off inhibits the build up of pressure at the tip reducing fracture propagation. The visocosity of the fluid resulted in much higher fractures with shorter half lengths. This is related to reduced fluid flow where an increase in viscosity leads to less pressure building up at the fracture tip, reducing propagation.

Geverik

In both wells penetrating the Geverik we observe longer fractures at EMO-01 compared to GVK-01. The overburden stress at the fracture center for GVK-01 and EMO-01 equate to 24.5 MPa and 64 MPa respectively. The Young's modulus at GVK-01 is 45 GPa higher than EMO-01 with a slightly lower Poisson ratio indicating that the Geverik interval present at GVK-01 is more brittle. Despite the latter location being more brittle, the much higher stresses resolved at EMO-01 resulted in fractures having shorter heights, longer half lengths and thinner widths.

Posidonia

Figure 13 displays the fracture characteristics simulated with MFrac of each well in terms of the ratio of length to height, with high ratios indicating longer fractures with shorter heights. We conclude that hydraulic fracturing will be most successful at the locations KWK-01, F17-03 or WAA-01. Additonally Table 5 in Appendix 3 shows that KWK-01 is characteristically brittle with a relatively high Youngs modulus of 34.17 GPa, Poisson ratio of 0.24 and a high fracture pressure of 9.5 Mpa due to low magnitudes of Sh_{min}.

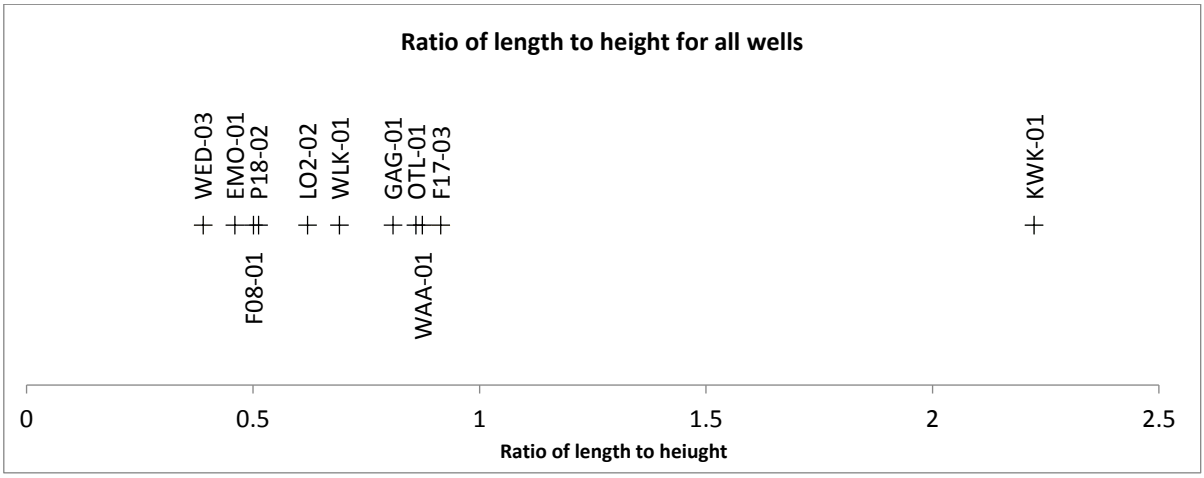

Figure 13. Displays the ratios of length to height at each well location with high ratios indicating long fractures.

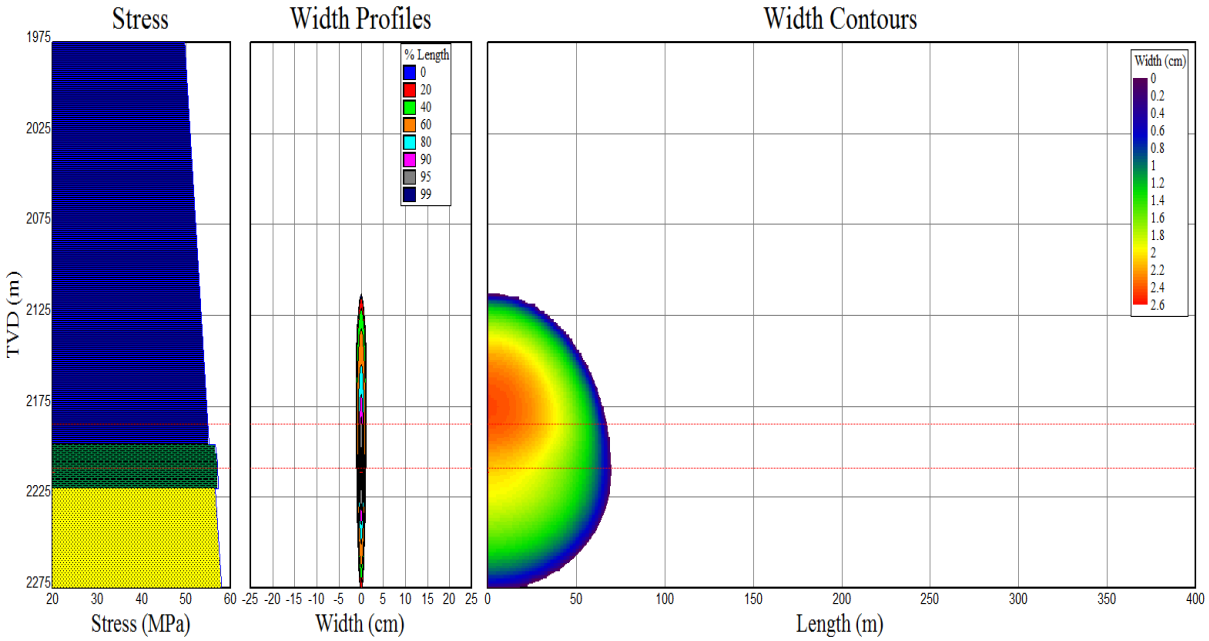

Figure 14. Plot showing the fracture dimensions modelled by MFrac for well WED-03 penetrating the Posidonia. Height of the line represents the height of the fracture whilst the cross lines represent (scaled) fracture width.

When comparing the Posidonia to the Marcellus, Woodford and Barnett Shales we find that the U.S shales are more promising for efficient fracturing than the Posidonia (Table 1). The differences to note are the higher brittleness indexes and the higher permeability found in U.S shales compared to the Posidonia. The average brittleness of the Posidonia is relatively low, below the recommended minimum of 30 cited by (Rickman, et al., 2008).

Table 1 A brief comparison of the Posidonia shales with U.S shales (Janzen, 2011)

	Thickness	Brittleness index (%)	Permeability m^2	TOC (%)	Maturity (Ro %)
Posidonia	30-100	18.5	1e-22 - 1e-18	3-12	0.5-1.3
Marcellus	75	30-40	1e-19 - 2e-16	6-12	1.1-1.7
Barnett	100	50	7e-20 - 1e-16	2-4	1.2-3.5
Woodford	80	65	5e-20 - 1e-18	4-10	1.2-3

Semi-analytical natural fracture model

The following presents the results of the semi-analytical fracture model. In this approach failure is induced on natural fractures following a power law distribution. The permeability was calculated from reactivated natural fractures and a weighted average between matrix and fracture permeability is applied to the reservoir. We validate the cumulative size of seismic moments by comparing the magnitude to the magnitude predicted from the total volume of injected fluids. We first present the results of a hypothetical scenario using the base case parameters in Table 2.

Subsequently we explain the results of a sensitivity analysis which varies the a exponent, maximum fault length, minimum fault length, number of faults, ratio of $Sh_{min}$to Sv, reservoir pore pressure and the change in pore pressure.

Simulations on a hypothetical reservoir

Input Parameters

For every model run we define two orientations of fractures. Faults had a higher probability of striking +/-10° to 360° and a lesser chance of striking +/-10° to 90°. The orientation of Sh_{min} and SH_{max} for each model run is parallel to the x (90°) and y (0°) directions of the model respectively.

Table 2 inputs used for a hypothetical scenario

	Base case
Power law distribution	
$a\ exponent$	2
Max fault length	30
Min fault length	10
Number of faults	100
Reservoir parameters	
Ratio Shmin – Sv	0.63
Pore pressure (MPa)	30
Increase in pore pressure (MPA)	15
Seismic moment - displacement	
Change in friction coefficient	0.2
Permeability	
k_m	2e-16
Shear modulus	3e11

The weighted probability for the orientation of faults results in two clear groups, represented on both the Mohr circles in Figure 15a and depicted by failure on faults in 3D on Figure 15b, where the reactivated faults dip parallel to Sh_{min}. Figure 15b highlights the larger earthquakes occurring on larger fault planes, indicated by larger spheres. This is confirmed by Figure 16 which displays the relationship between both fault length, displacement and the seismic moment magnitude. We find a clear positive correlation in both instances and conclude that the seismic moment is more sensitive to the fault length. The simple reason for this relates to scaling of fault lengths used in the seismic moment equation. The variation in fault length is much greater than that that of displacement and therefore we observe a stronger trend.

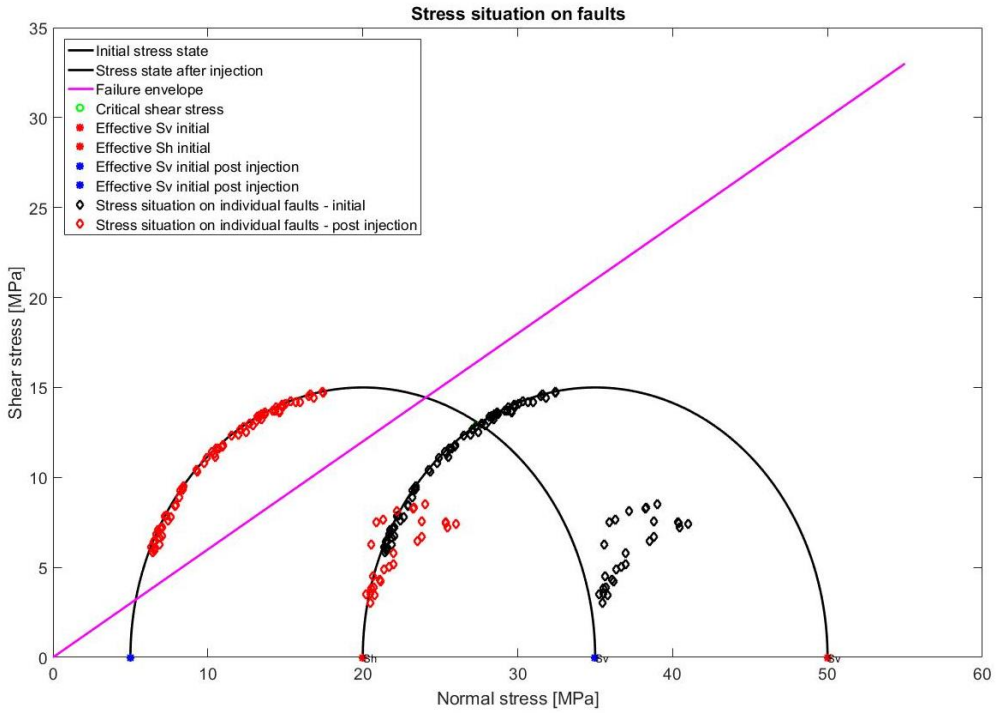

A

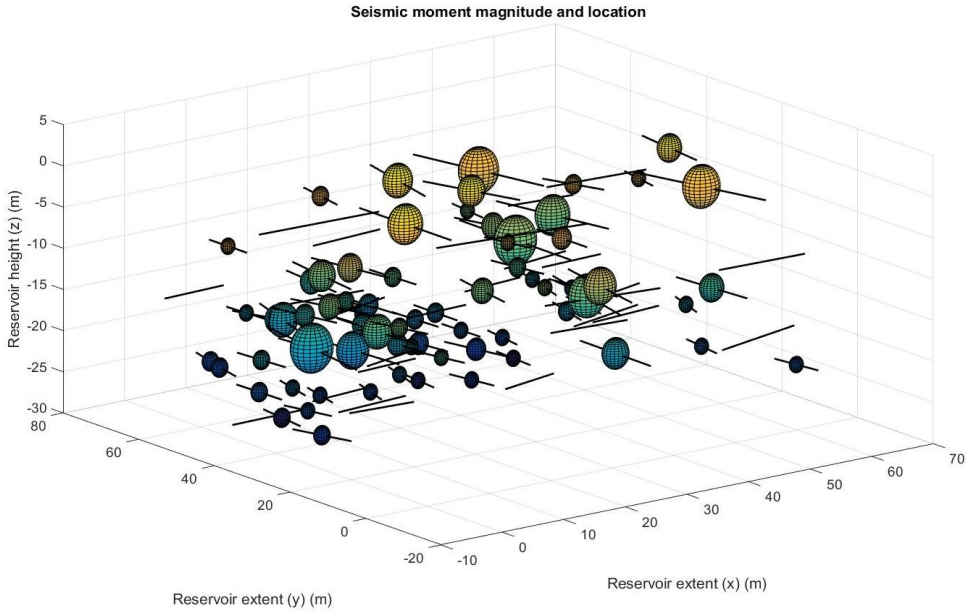

B

Figure 15a. displays a hypothetical scenario whereby the initial effective overburden pressure is 50 MPa, Shmin 20 MPa and the pressure is increased throughout the reservoir by 15 MPa, resulting in reactivation on faults orientated optimally for failure. Figure 15b displays fault strikes in 3D indicating seismic moment magnitudes by the size of the sphere

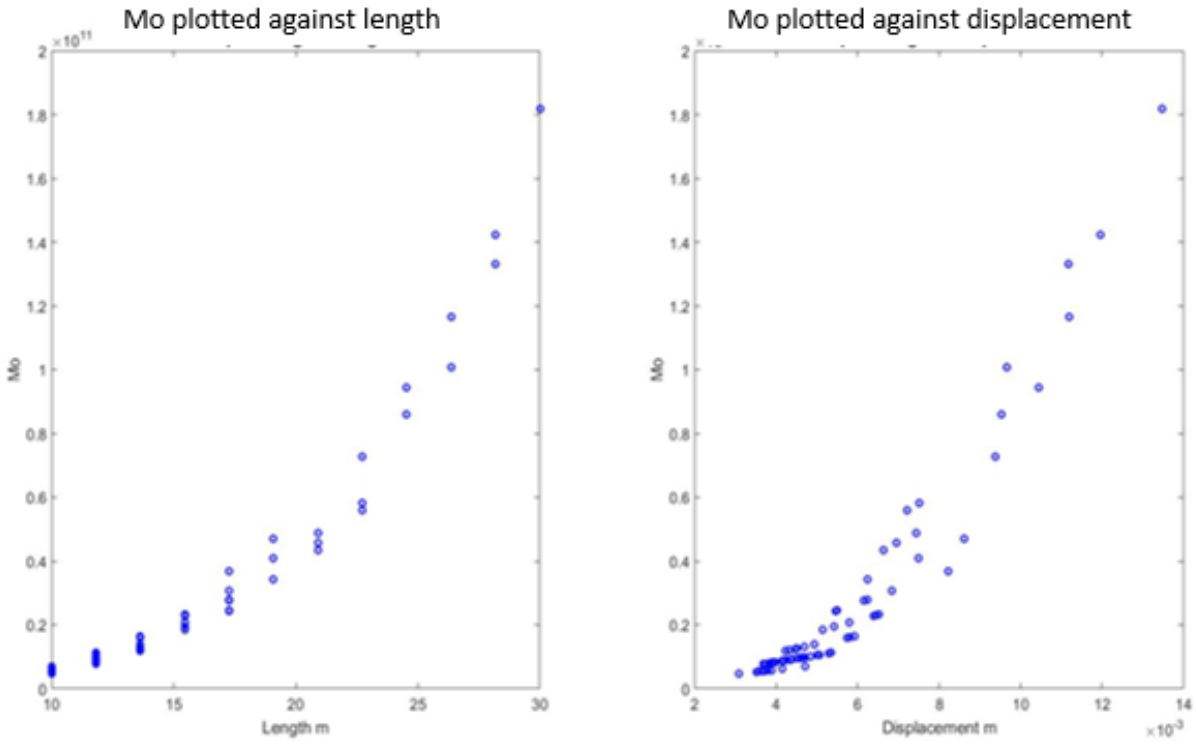

Figure 16. Shows the seismic moment against both fault length and displacement length

To test if the distribution of the magnitude of seismic moments were realistic we converted moment into Guttenberg-Richter M_l magnitudes and fitted with the G-R relation, Figure 17. We observe a good fit between the seismicity induced on faults in the model, and a linear relation in log frequency-log magnitude plots as suggested by Gutenberg-Richter. Typically, b values range between 1 and 3 and for simulations with base case inputs we fit a b value of 2.9. Higher b values indicate a greater number of smaller events.

A comparison of the relative magnitude of events was slightly more problematic due to the availability of data Figure 18. We compared modelled seismic moment magnitudes with the maximum seismic moments recorded at several locations during hydraulic fracturing, fluid circulation in enhanced geothermal systems (EGS) and waste water disposal McGarr (2014). Figure 18 shows that events were between $10^{10} - 10^{18}$. Typical maximum values for hydraulic fracturing are around 10^{12}, whilst the model calculates the largest event as $1.8{\times}10^{11}$.

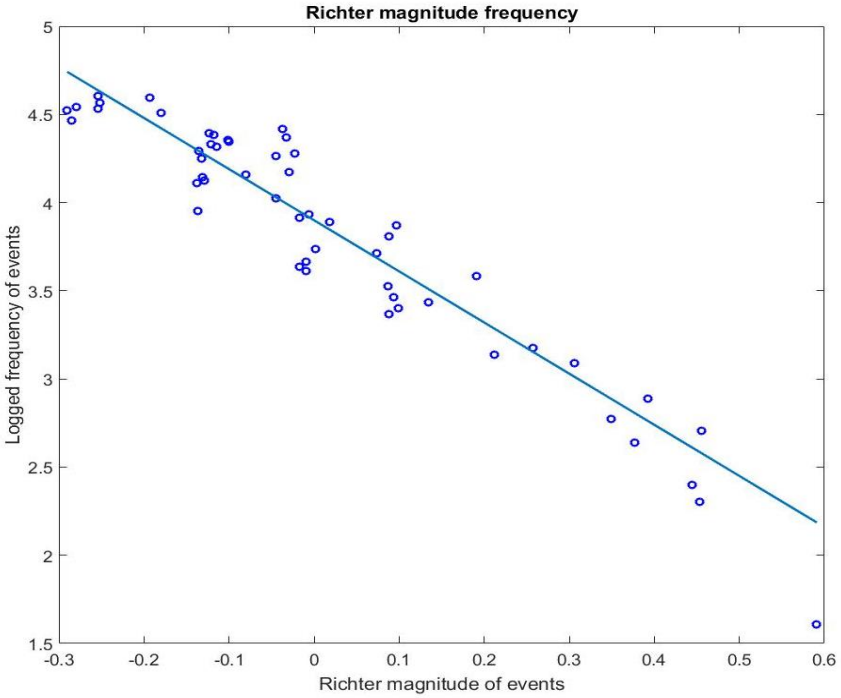

Figure 17. GR Magnitude frequency of events plotted against a GR relation - b coefficient of 2.5

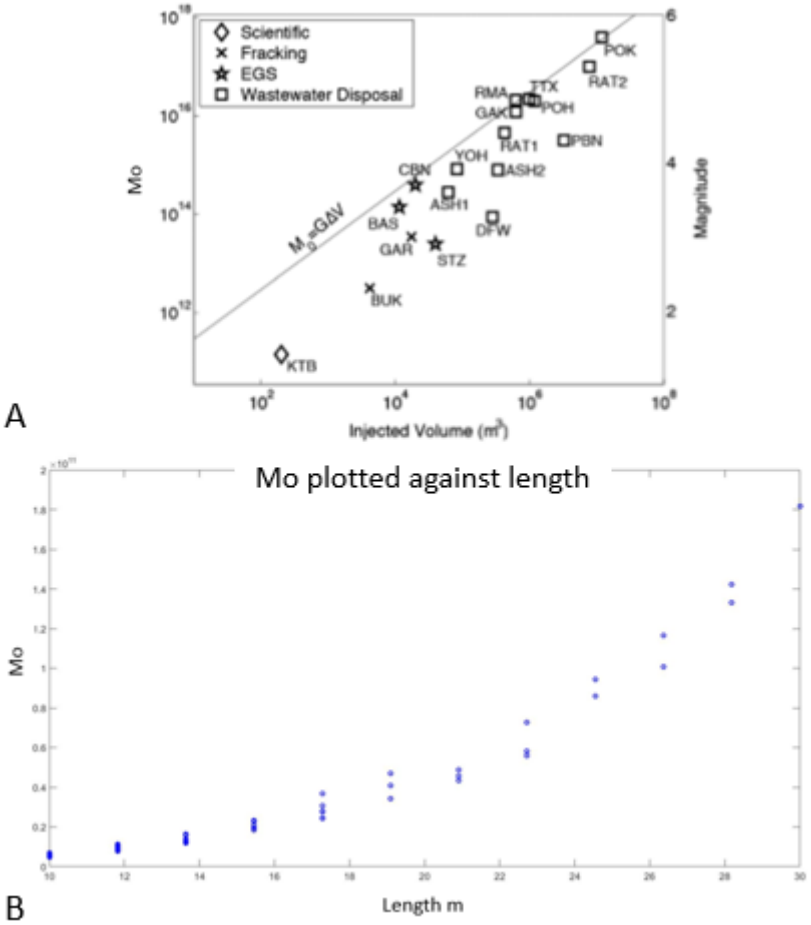

Figure 18a recorded seismicity during fluid injection for fracturing, waste water disposal and geothermal facilities compared with Figure 18b model magnitudes.

Permeability of the reservoir

The fracture permeability was controlled by the combined fracture aperture in normal and shear, calculated using normal stress and displacement respectively (Equation 21 & Equation 22.). Figure 19 shows fracture permeability against fracture combined aperture, fracture permeability when b_s is held constant and when b_n is held constant. The results show that the shear opening of fractures is the dominant variable in controlling total aperture under current assumptions. The simple explanation for this is that the volume of shear aperture is much larger than the normal component, for example normal aperture never exceeds 3.75x10^{-4} m, whilst shear aperture was larger than 8x10^{-4} m (Figure 19,Figure **22**). We assume a constant dilation angle of 3° meaning that the controlling variable for shear aperture was displacement, which in turn is controlled by the stress drop and fracture stiffness. The fracture stiffness for each fault is dependent on the length, whilst the stress drop is controlled by the change in effective normal stress, since the change in the steady state friction was assumed to be 0.2 on every fault. This explains the trend in Figure 20 where we observe a positive correlation between the change in effective stress, fault length (radius) and the permeability. The impact of linear binning and fault length on the permeability calculation is clear from the notable steps in lengths Figure 20. Since Sh_{min} and *Sv* were held constant on all faults in the reservoir the orientation of faults controls the extent of the change in normal stress, and therefore normal and shear aperture. Collectively this meant that fracture permeability was greatest on longer faults dipping towards Sh_{min}, shown in Figure 19 & Figure 20.

As previously stated fault length was one of the controlling variables of seismic moment magnitude and we find a positive correlation between the magnitude of an earthquake and permeability Figure 20.

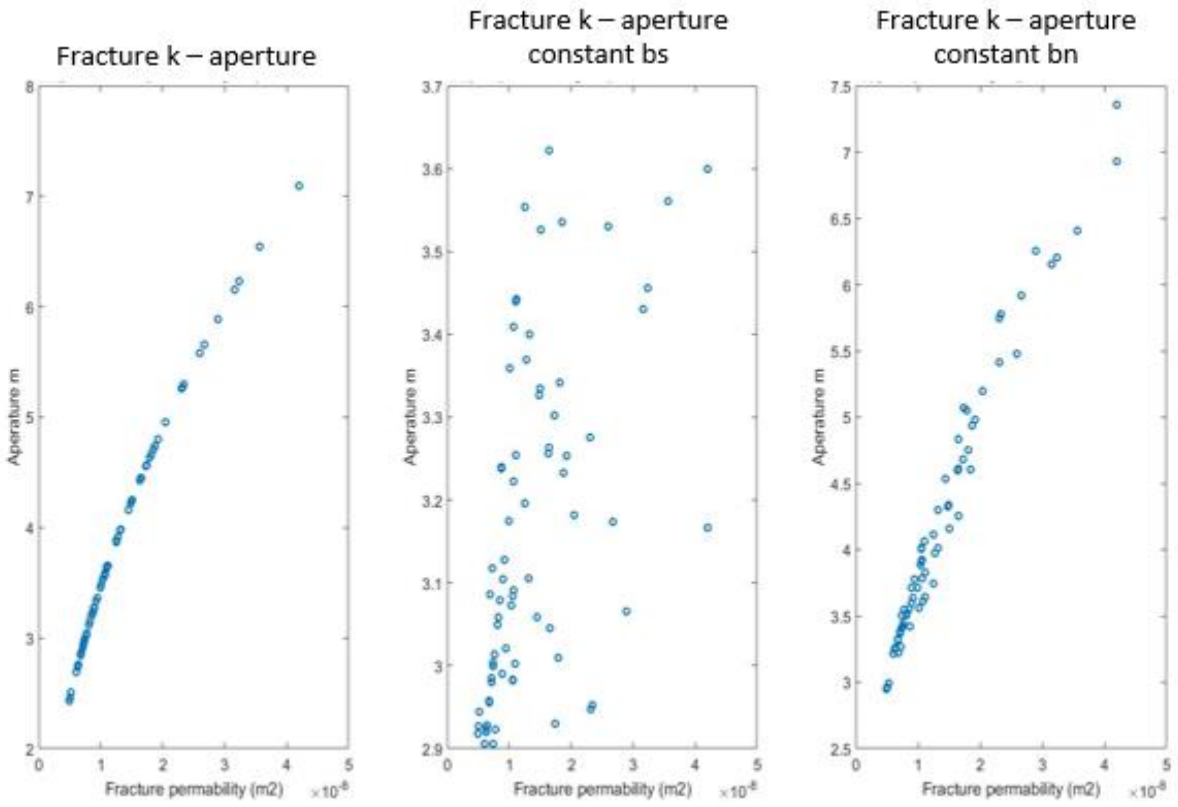

Figure 19 from right to left shows the relationship between fracture aperture and permeability in x,y,z directions with combined effects, permeability when bs held constant and bn held constant.

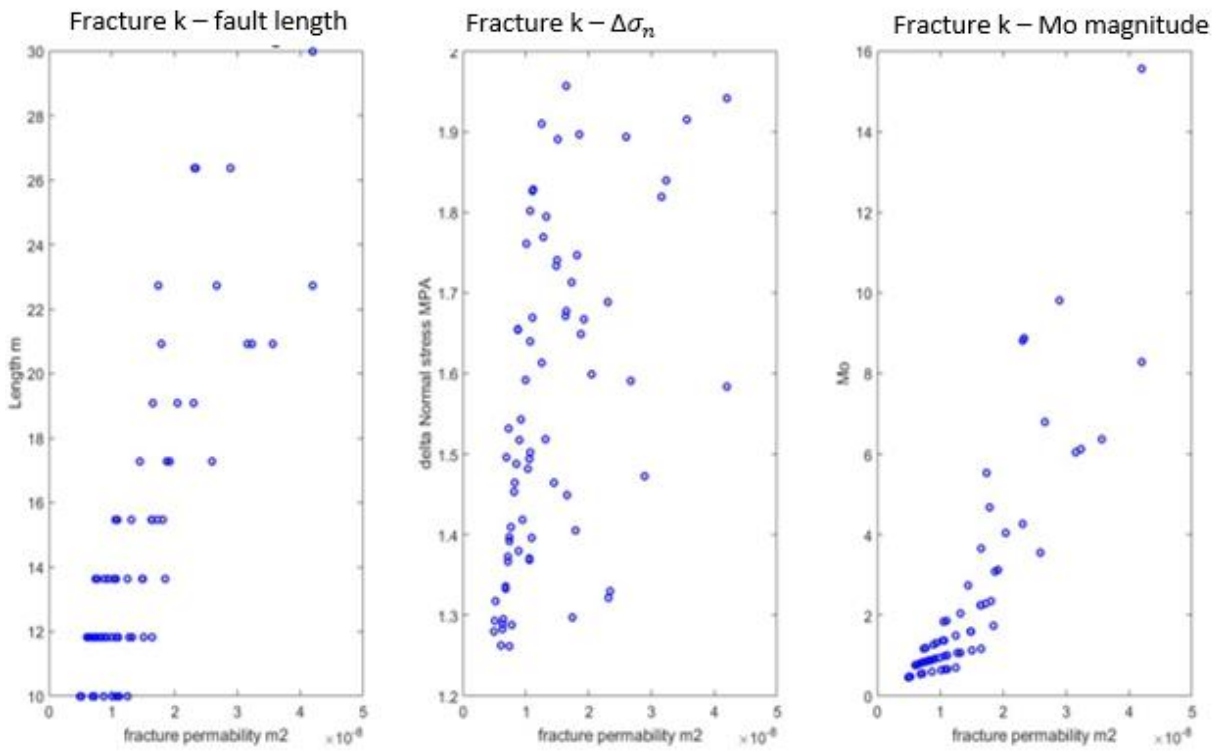

Figure 20. Fracture permeability plotted against, fault length, change in effective normal stress and moment magnitude.

Fracture permeability was decomposed into a permeability tensor and transformed according to the orientation of the fault to the coordinates of the model. The relationship between the principal permeability directions and fault dip and dip direction was solved analytically and represented in Figure 21. Figure 21 presents a simplified analytical solution assuming a scenario with 360 faults, whereby the orientation systematically increases by 1° from 0-360°, whilst holding fault dip at 0°. This initial run transformed the permeability tensor displayed below (Equation 28) and shows how the dominant permeability direction changes with the orientation of the fault, signified by the blue and red diamonds (Figure 21**)**. In the second simulation, the fault orientation was held constant and the dip was varied from 1°-90°. Figure 21 displays the positive relationship between the dip of the fault and permeability in the k_{zz} direction (green), peaking at vertical.

Equation 28

$$k = \begin{bmatrix} 5 & 0 & 0 \\ 0 & 1.7 & 0 \\ 0 & 0 & 0.5 \end{bmatrix}$$

Figure **22** shows the magnitude of the principal permeability directions on reactivated fractures calculated by the model. The conditions set for the model ensure that fracture strike varies +/-15° from the y axis and dip from 50° to 80° (base case). This explains why permeability in the k_{yy} direction is notably higher than in the k_{xx} and k_{zz}. However, we observe no clear relationship in the principal permeability directions as anticipated from Figure 21. This is because when solving Equation 28 analytically we assumed a constant permeability tensor for every fault. For the model simulation presented in Figure **22** each fault had its own fracture permeability. Thus, the varying size of fractures apertures makes it difficult to distinguish notable trends.

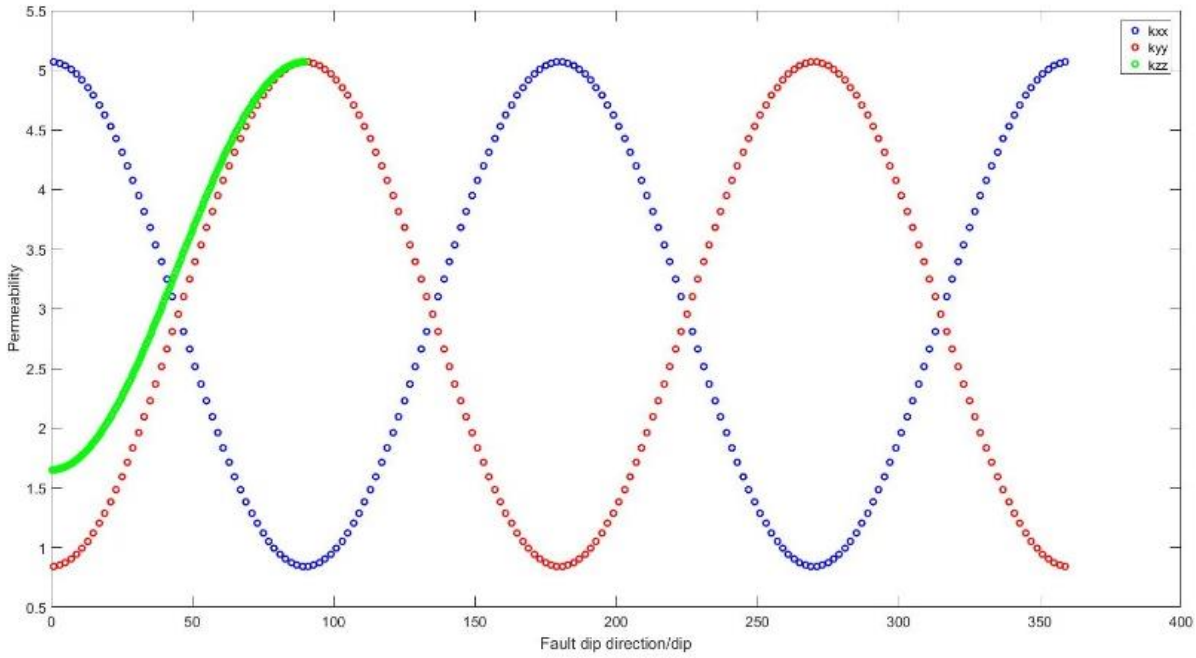

Figure 21. Analytical solution of the permeability tensor highlighting how the dominant permeability direction changes with orientation

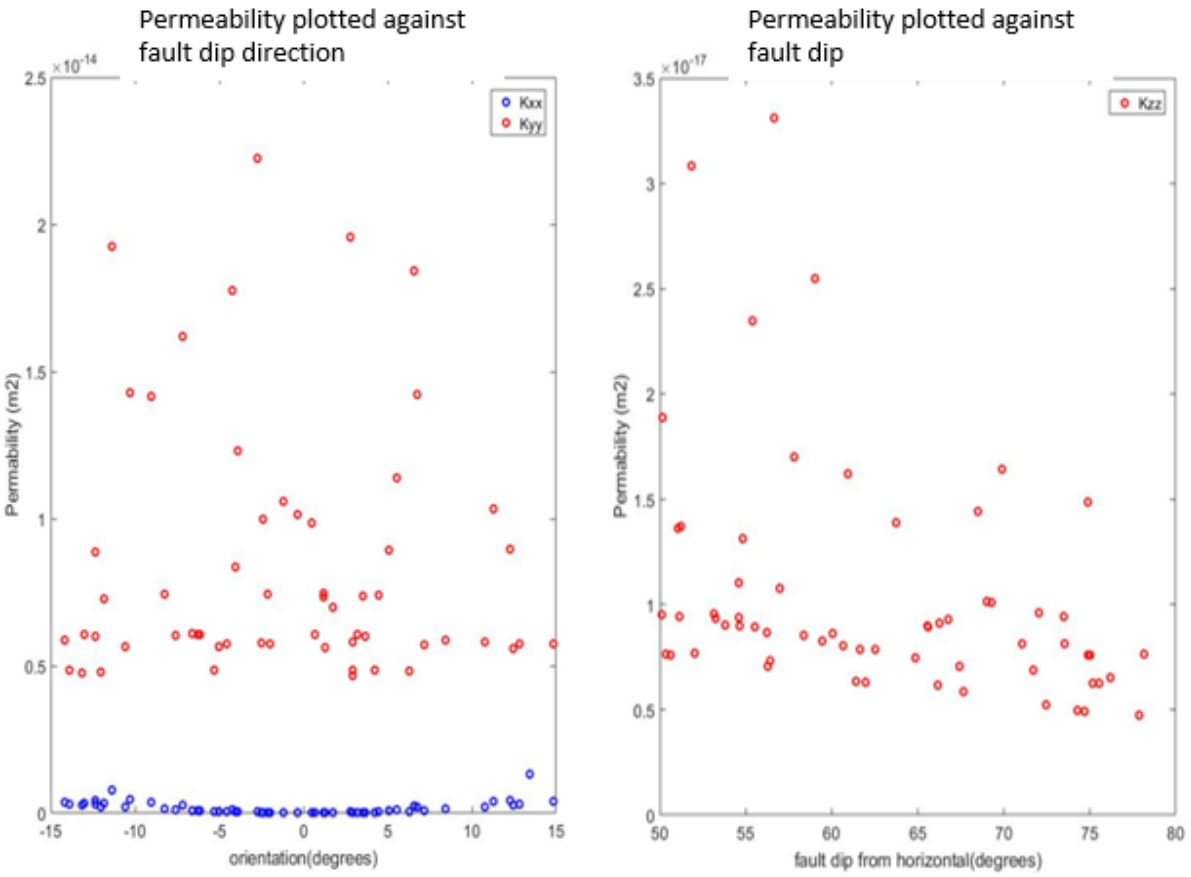

Figure 22. Shows the trend in permeability in the k_{xx}, k_{yy} (left image) and k_{zz} (right image) direction.

Validity of modelled cumulative seismic moment

The analytical model represents a simplified scenario whereby a uniform pressure increase is assumed resulting in a cumulative seismic moment of 1.4940e+12. In order to test this model, we use the method of McGarr (2014) to compare the modelled cumulative seismic moments with the predicted moments associated with the total injected fluid volume. As previously stated McGarr (2014) assumes that all faults will be reactivated following injection and represents an upper bound of expected cumulative seismic moment.

Flow rates were calculated and importantly the fluid volume required to induce failure. Fracture permeability was estimated from reactivated faults following a uniform rise in pressure of 15 MPa. We then used this permeability map to model fluid flow and pressure changes, thus adopting a reverse approach.

The results are summarised in Figure 23 and show the time taken for pressures to increase up until the yield stress at the outer edge of the ellipsoid. One would expect the pressure required for failure at the outer edge to be reached fastest in the y direction, due to higher permeability and flow rate. The trend in time taken for pressures to increase is related to the distance from the centre to the edge of the ellipsoid, where distances were furthest in the y direction. Of note are the various pressures required for reactivation at the edge of the ellipsoid which range from 15-19 MPa respectively. Using the time taken for this pressure increase and the flow rate the cumulative fluid volume was calculated, presented in Table 3. Table 3 also includes the cumulative seismic moment calculated using McGarr (2014) and total fluid volume compared with the model's total seismic moment. We find a reasonable agreement between the seismic moment calculated by the model and predicted magnitudes following McGarr (2014), see Table 3. The volume of injected fluid calculated by the model is a small estimate when compared to other studies where pumping time can last for several days. Simulations from the analytical model were conducted in a cube measuring 60mx60m. Therefore, the time taken for the pressure to reach the magnitudes required for failure at the edge of the ellipsoid was achieved in around 250 seconds.

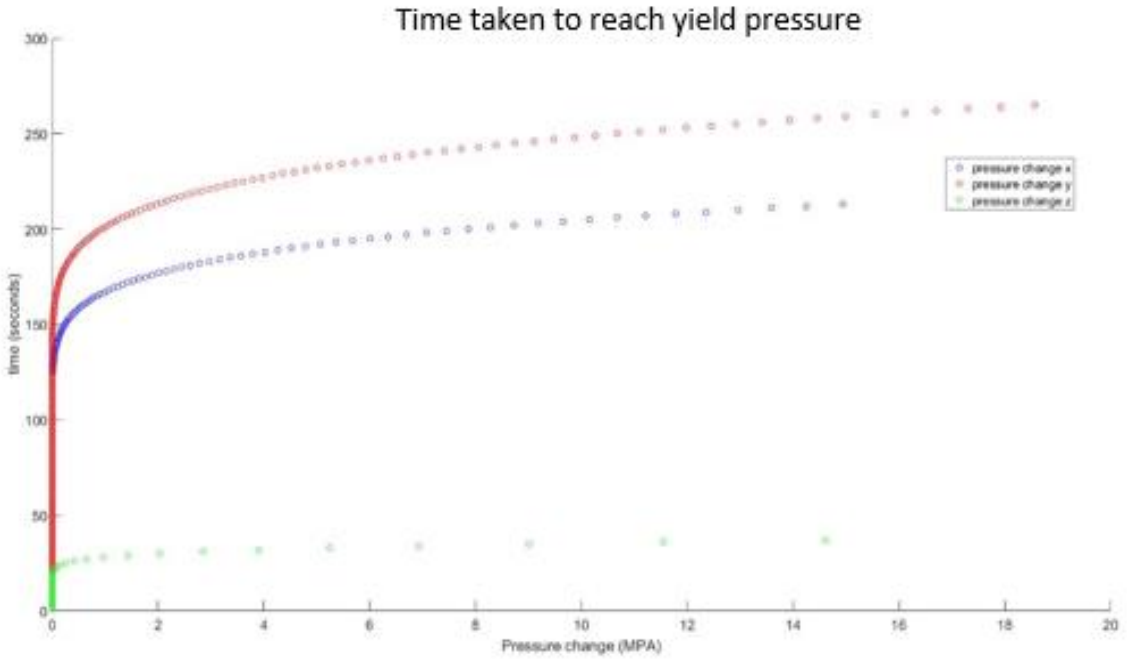

Figure 23. pressure change though time in x, y, z directions.

Table 3. Presents the model results comparing seismic moment magnitudes based on both fluid and fracture volume and total seismic moment calculated by the model.

TOTAL FLUID VOLUME	**40.61 m^3**
TOTAL FRACTURE VOLUME	**4.9018 m^3**
MCGARR (2014) SEISMIC MOMENT BASED ON FLUID VOLUME	**2.4370e+12 M_o**
CUMULATIVE SEIMIC MOMENT	**1.7226e+12 M_o**

Sensitivity analysis

The following presents the sensitivity of the cumulative seismic moment to the variables highlighted in Table 4. Each variable was varied between a maximum and minimum value whilst holding all other variables constant at base case values. For each model run we retain the same dominant and subordinate fracture orientations.

Table 4. Showing the different parameters varied in the sensitivity analysis

	Low case	***Base case***	***High case***
Power law distribution			
a	2.9	2	1.1
Max fault length	15	30	45
Min fault length	5	10	15
Number of faults	50	100	150
Reservoir parameters			
Ratio Shmin to Sv	0.73	0.63	0.53
Pore pressure (MPa)	25	30	35
Increase in pore pressure (MPA)	10	15	20

Reservoir conditions

Figure 24 captures the sensitivity of cumulative seismic moments to the ratio of Shmin – S*v,* pore pressure and the increase in pore pressure. We find a negative correlation between the in-situ pore pressures and cumulative seismic moments. It was expected that increasing the in situ pore pressures would decrease the effective normal stresses, leading to a higher number of critically stressed faults, and therefore a higher cumulative seismic moment. We observe this trend because of the way the model calculates displacement on a plane. An increase in reservoir pressure will result in less effective normal stresses and crucially lower stress drops, reduced displacement lengths and smaller moment magnitudes. However, this trend is not found when altering the change in pore pressures, indicating that the model is more sensitive to the selection of initial reservoir pressure.

We find a positive trend between the ratio of Sh_{min} to *Sv* whereby larger seismic moments were realised when the ratio was higher. The impact of changing stress ratios can be graphically represented on a Mohr circle whereby higher ratios result in smaller circles and higher normal stresses. The higher normal stresses stabilise the faults meaning that a higher pore pressure is required to induce failure. However once movement is initiated, larger effective normal stresses increase the stress drop on each fault, again increasing the displacement length and associate moment magnitude.

Power law distribution

Figure 25 presents the sensitivity of cumulative seismic moments to the fault total, maximum and minimum fault lengths and the *a* exponent. As expected we observe a positive relationship between the total number of faults and cumulative seismic moment.

Comparing the selection of the minimum fault length and the maximum fault lengths yields a stronger correlation when varying the minimum fault length. For clarity, when calculating the power law distribution, we use the minimum fault length to generate a frequency of faults at each length, achieved through linear binning. We then assign the maximum fault length and fit the distribution accordingly. The reason for the trends observed in Figure 25 is related to the way in which the power law generates frequency distributions. As such, a much higher quantity of small faults is given than larger. By increasing the length of smaller faults, we effectively increase length on more faults compared to increasing the size of larger faults. This can be thought of in terms of cumulative length, whereby the cumulative length is larger if the minimum fault length is increased rather than the maximum.

The choice of the *a* exponent has the greatest impact on cumulative seismic moment, particularly between 1 and 1.5. The *a* exponent is the main controller over the amount of faults at each length, where lower values of *a* result in a larger proportion of larger faults.

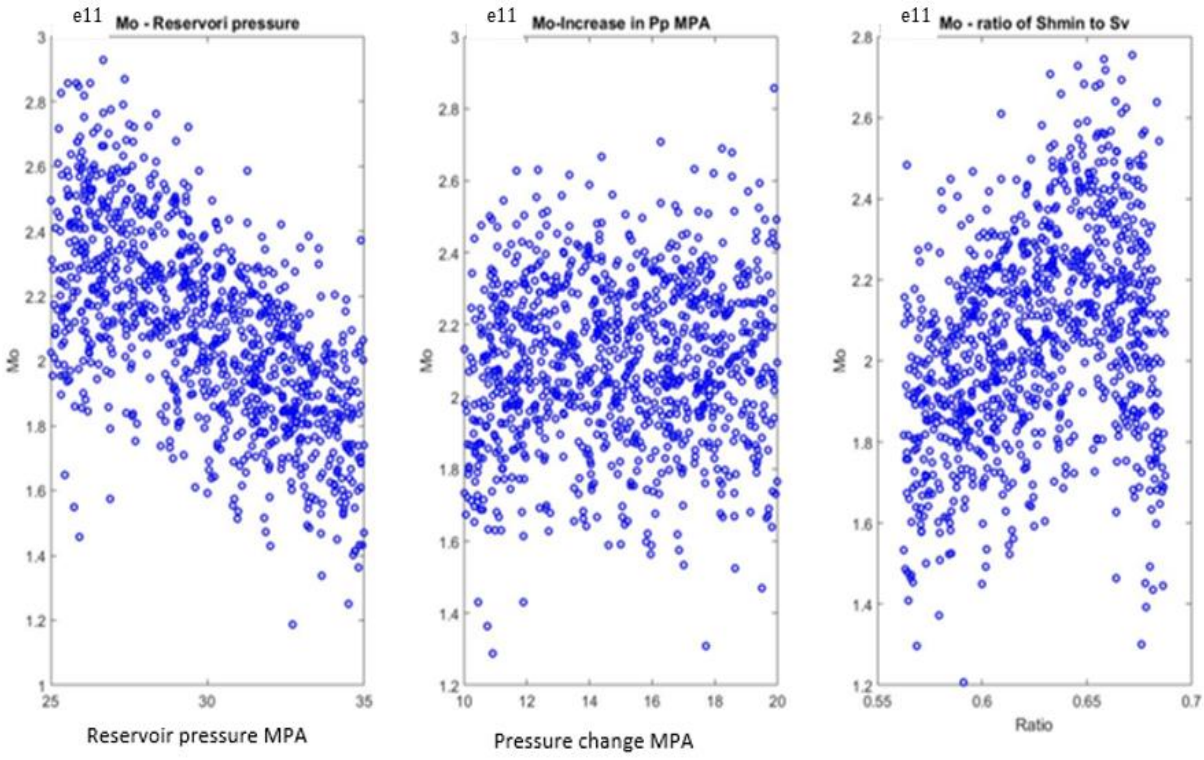

Figure 24 plots shows the results of a sensitivity analysis where reservoir pressure, pressure increase and the ratio of Sv to Sh_{min} were compared to the cumulative seismic moment

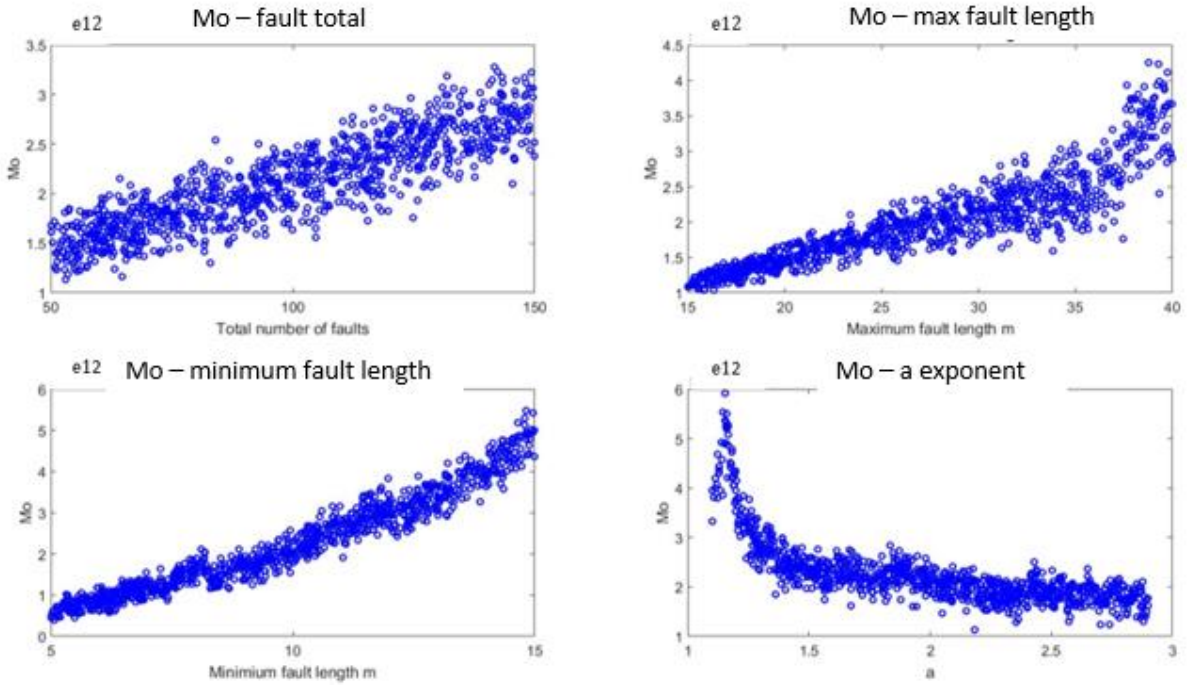

Figure 25 plots shows the results of a sensitivity analysis where fault total, max length, min length and a coefficients were compared to the cumulative seismic moment

Discussion

The reason for forward modelling is to characterise how a reservoir will respond to hydraulic stimulation. Subsequently, providing a tool to aid researchers when designing an optimum treatment schedule and inferring the production of hydrocarbons. We discuss the results of both modelling approaches and their limitations separately. After, comparisons between both approaches are made and we suggest how forward both modelling approaches relate to treatment designs and comment on future research.

Elementary modelling approach (Mfrac)

From Figure 7 - Figure 11 we conclude that in a less brittle reservoir subject to low stress, fractures will be characteristically taller in height, narrower in width and shorter in length. Conversely, in more brittle and highly stressed reservoirs fractures will have shorter heights, narrower widths and longer lengths. Fractures which are long and narrow are regarded as the most optimum fractures in terms of yielding the best production rates of hydrocarbons (Holditch, et al., 1978).

The results showed that lengths slightly decreased and widths increased with an increased Poisson ratio and we find no trend in the ratio of height to length. Conversely, from an increased *E* we observe a negative trend in width and a positive linear relationship between length and Young's modulus. We also model high ratios of length to height with increasing Young's modulus.

Rickman (2008) states that the Poisson's ratio is particularly relevant to the ability of a rock to fail, as such lower Poisson ratios mean that rocks are more prone to failure. Poisson's ratio assesses the lateral deformation, i.e. compressing a rock in one direction will result in expansion in perpendicular directions. Whilst the Young's modulus describes the stiffness of the material, with larger values indicating stiffer rocks which will fail in a more brittle manner. Our results agree with Gidley et al. (1989) who also noted that fracturing rocks with higher Young's moduli resulted in long narrow fractures. These findings question Grieser et al. (2007) whom reason that both a high Young's modulus and low Poisson's ratio is associated with a good brittleness index. Ter Heege et al. (2015) state that the brittleness index is significant for 'sweet spot' identification, used to highlight the best areas for shale gas extraction. We argue that the magnitude of Young's modulus is more important when identifying areas which will respond optimally to stimulation. The stark differences in Youngs modulus at the different well locations result from the composition of the shale. For example, comparing Geverik locations GVK-01 and EMO-01 we suggest that GVK-01 may have a higher density of brittle minerals such as quartz and dolomite. This is somewhat unexpected as the deeper shale present at EMO-01 should be more mature and undergone more diagenesis, thus more brittle. However, it is important to emphasize that both well locations are in different basins with GVK-01 situated in the West Netherlands basin and EMO-01 in the Central Graben. Therefore, one would expect different sedimentation patterns and a different burial history resulting in different temperature and pressure histories.

Poisson ratio also featured in this study when calculating Sh_{min} from Eaton's (1969) equation based on pore pressure, Sv and the Poisson's ratio. As such we find larger magnitudes of Sh_{min} with increased Poisson ratio. From Equation 11 we find that higher magnitudes of Sh_{min} resulted in longer fractures. This is because widening is restricted by the magnitude of Sh_{min} and fracture heights were fixed resulting in longer fractures. Using Equation 12 we also observe higher ratios of length to height with increasing Sh_{min}. This trend was not always found when modelling with MFrac. For example, the impact of higher stress within the reservoir is particularly prominent at well WED-

03. From MFrac longer fractures were most numerous in regions with lower magnitudes of horizontal stress due to the containment of fractures. The stress profiles in Figure 14 show stresses are much higher in the Posidonia than in the confining Lower Werkendam Member (below) and Aalburg Formation (above). Cardott (2008) reasons that having a sufficient fracture barrier is very important and shales with a higher stressed cap rock respond better to stimulation. For example, Hammack et al. (2014) describe how the Marcellus Shale is overlain by the higher stressed Tully Limestone. Subsequently, the micro seismicity generated during 56 treatment stages was largely contained within the reservoir (Hammack, et al., 2014). Higher stress within the reservoir compared to confining layers limits the effectiveness of stimulation, as energy, fluid and proppant are wasted when fractures propagate out of the intended zone (Speight, 2017). Conversely, in higher stressed reservoirs the yield stress is higher meaning that more energy is required for tensile failure (Holditch, et al., 1978). Therefore, when selecting an appropriate area for shale gas extraction we argue that it is most important to identify regions which are both adequately stressed and are confined by higher stressed layers. In these areas there is a better chance of more optimum longer fractures developing from hydraulic stimulation.

Based on the results from this study, KWK-01 represents the most promising area for shale gas extraction. Janzen (2011) reason that the area around Boxtel (Netherlands) is the most promising location in terms of the reservoir properties (e.g. depth, thickens, fracture density), shale composition (e.g. TOC, clay and sand minerals) and shale properties (e.g. porosity, permeability, brittleness and thermal maturity). This area is located just 10 km southeast from KWK-01, therefore we expect the shale to have a relatively high brittleness index and low magnitudes of $Shmin$, responding with longer fractures. The higher brittleness in this region is likely to be associated with a higher sand content and more established diagenesis due to higher maturities.

Limitations

The approach of Mfrac has the obvious limitation that no natural fractures are modelled and simply predicts only the height and length of tensile fractures. Ter Heege (2016) argues that permeability through the reservoir is largely controlled by the presence of natural fractures. We argue that using this approach poorly represents fractured reservoirs and will underestimate reservoir permeability.

Semi-analytical natural fracture model

The following discusses the applicability of using a power law distribution to describe the distribution of fault sizes in the reservoir. Studies such as Bour and Davy (1999) argue that the frequency distribution of fault lengths measured from outcrop data follows a power law distribution. Among others Massiot et al. (2015) used a power law distribution to characterise the lengths of faults and fractures within a geothermal reservoir. However, Nicol et al. (1996) question whether the power law relationship exists in nature. Speculation arises when observing the different power law exponent values from sampling outcrop and seismic data. Nicol et al. (1996) argue that fault sizes do not follow a power law distribution, especially over large size ranges. The analytical model has shown that the induced seismicity on faults which follow a power law distribution follow a similar size distribution based on GR relations. Natural earthquakes follow a log normal distribution and Davies et al (2013) reason that human induced seismicity is no different. The most important parameter when fitting the GR relation is the magnitude of the b coefficient, which controls the frequency magnitudes of events. For example, Maxwell et al (2009) set the b coefficient to 2.86 for the Barnet shale. Zhu and Wilson (2016) calculated b values during treatment stages at three different wells in the Marcellus Shale, finding an average b value at the three wells of 2.7, 2.8 and

2.6 (Zhu & Wilson, 2016). We fit a GR b value of 2.9 onto Figure 17 and conclude that the model creates a robust distribution of magnitudes under the current model assumptions.

The model also estimates reasonable seismic moment magnitudes but we acknowledge that magnitudes seem low when compared to those recorded at waste water and EGS facilities. The reason for larger events recorded at EGS may be because of greater thermo-elastic stress changes, which can often result in larger events, particularly in the medium to long term (Gaucher, et al., 2015). Large events are also found in waste water projects relating to the huge volumes of injected fluids (McGarr, 2014). Compared to other fracturing projects, magnitudes are still slightly lower. We argue that this is because the events shown in Figure 18a represent maximum events during treatment, thus smaller events are underrepresented. Additionally, the cumulative seismic moment predicted by the total injected fluid volume is in good agreement with the total seismic moment calculated by the model. We conclude that the semi analytical model creates a robust size frequency of earthquake magnitudes but we stress that they are heavily dependent on the power law inputs.

Apparent from the sensitivity analysis is the strong dependence that cumulative seismic moments have on the input variables for the power law distribution. We argue that the main controller of the size and distribution of the seismic moment magnitudes is the distribution of fault lengths and displacement. Clark and Cox (1996) argue that fault size influences displacement, whereby displacements steadily increase proportionally with fault length. This is expected as increased fault lengths can accommodate more displacement. We used a simple linear relationship between fault length and displacement and although a trend is noted we suggest that it is more complex. For example, physical influences such as lithology type, layering and thickness can restrict the validity of scaling displacements (Bonnet, et al., 2001).

Clustering of fractures is often observed in reservoirs and explains why studies such as (Hammack, et al., 2014) resulted in concentrated areas of micro seismicity. We devised an approach which results in areas of high fracture density, a feature which was lost when a bulk permeability tensor was calculated. Future studies may wish to create a strategy to map the permeability of fractures, incorporating zones of high fracture density. Inclusion of this phenomenon in flow models may improve the estimation of flow rates and has applications for shale gas extraction (sweet spots) and geothermal energy production.

Limitations

The model presumes every critical fault would fail seismically, omitting velocity strengthening faults and assuming all faults weaken. Future research may wish to consider the following. Firstly, introducing frictional a and b parameters and coseismic velocities, so that a proportion of critically stressed faults will be aseismic. Several faults may also result in larger displacements due to a greater change in the coefficient of friction (Di Tioro, et al., 2011). Secondly, we suggest adding a probability function to each fault controlling the likelihood of failure, once the fault is critically stressed.

Comparison of models

Despite the stark differences in modelling techniques some commonalities between the two are visible. The following discusses this and comments on how a fractured reservoir is likely to respond to pore pressure changes and remarks on the impacts to permeability and fluid flow.

Simulations from the elementary modelling approach indicate that higher stressed reservoirs promote longer tensile fractures. The semi analytical model indicates that an increased ratio of Sh_{min} to Sv will result in larger moment magnitudes. To explore the ratio Sv was held constant and Sh_{min} was varied. With increasing magnitudes of Sh_{min} displacement distances are larger, resulting in larger shear apertures, enhancing fracture permeability. From both modelling approaches we conclude that the production of hydrocarbons from a fractured reservoir will be more successful from highly stressed reservoirs.

From the simulations in MFrac we have shown that the operational parameters used during treatment i.e. injection rate, volume fluid viscosity and leak off, had a large control on the tensile fractures. Fluid injection rate and viscosity controlled the height, length and width of fractures. Where high injection rates and viscous fluids resulted in high and wide fractures. Modelling fluid flow with the semi analytical model indicates that pressure changes, particularly around the well result in tensile failure, ensuing from low permeability hindering pressure dispersion rates. We argue that reducing the injection rate and viscosity of fluids will result in lower pressure increases and more fractures reactivating in shear. In summary, we suggest that a gradual build up in pressure will result in longer tensile fractures and a larger portion of fractures reactivating in shear. The analytical model shows that increased shear opening of natural fractures (under model conditions) had a positive impact on fracture permeability. From both simulations, we argue that in low permeability reservoirs reduced injection rates and fluid viscosity may result in improved reservoir stimulation.

Mfrac simulations showed a positive relationship between the volume of injected fluids and the volume of tensile fractures and in optimum conditions this transpires into increased lengths. From the semi analytical model, we expect greater predicted cumulative seismic moments with increased fluid volume. This is supported by the study of Wassing et al. (2014), where an increased fluid volume resulted in larger rupture areas of fault planes, explaining the additional seismicity. We argue that there is a connection between increased cumulative seismic moment and permeability. Research by Holditch et al. (1978) correlates total injected fluid volume with increased fracture length and production. From this we suggest that to a certain extent an increase in fluid volume will improve reservoir productivity in both modelling approaches.

Conclusion

This study analysed the in-situ stresses and elastic constants in twelve wells to model fracture dimension using the MFrfac simulation tool. The well locations were selected to represent both the Geverik and Posidonia shale spatially and of the twelve wells, two penetrated the Geverik and the remainder the Posidonia. We conclude that the width of fractures is largely controlled by the Young's modulus and stress, such that layers subjected to high stress and high Young's modulus exhibit narrow fractures. More specifically, the efficiency of stimulation increased as less of the fracture propagated into the surrounding lithology. Furthermore, the strong correlation between volume and leak-off suggests that the leak-off had the biggest impact to the fracture dimensions. Using this method provides a useful depiction of how the reservoir may respond to stimulation, yet ignores natural fractures. This study has emphasised that fluid flow is largely controlled by the presence and reactivation of natural faults fractures. We have shown that one can indeed use a power law distribution to characterise the occurrence of faults within a reservoir when compared to Guttenberg Richter plots and moment magnitudes from other studies. Furthermore, we provide a method of inducing failure and modelling fluid flow within a stimulated reservoir volume, where cumulative seismic moments and fluid volumes show reasonable agreement. We also introduce a method for weighting the distribution of faults and fractures within the reservoir to better represent

nature. One of the difficulties found when using this simplified approach is characterising the connectivity of natural fractures, thus we used a weighted average between the matrix and fractures. From both modelling approaches we acknowledge the stark differences in approaches regarding the modes of fracturing. We suggest that a hybrid model of the two will best represent fractured reservoir modelling.

Acknowledgements

The thesis was supported by TNO and the university of Utrecht. Thank you to the people who helped me particularly my supervisor Maartje Houben and special thanks to Jan Ter Heege for his supervision during this study.

References

Aliouane, L. & Ouadfeul, S. A., 2014. Sweet spots discrimination in shale gas reservoirs using seismic and well-logs data. A case study from the Worth basin in the Barnett Shale. Volume 59, pp. 22-27.

Amann-Hildenbrand, A., Ghanizadeh, A. & Kross, B., 2012. Transport properties of unconventional gas systemes. *Marine and Petroleum Geology,* Volume 31, pp. 90-99.

Angus, D. et al., 2010. Modelling microseismicity of a producing reservoir from coupled fluid-flow and geomechanical simulation. *Geophysical Prospecting,* Volume 58, pp. 901-914.

Baig, A., Lunen, E. & Hendrick, J., 2012. Towards Using Seismic Moment Tensor Inversions to Infer Reservoir Rock Properties. *Geoconvention 2012,* Volume `1, pp. 1-4.

Balan, B., Mohaghegh, S. & Ameri, S., 1995. State-Of-The-Art in Permeability Determination From Well Log Data: Part 1- A Comparative Study, Model Development. *SPE,* pp. 17-21.

Bergen, F., Zijp, M. & Kombrink, H., 2013. Shale Gas Evaluation of the Early Jurassic Posidonia Shale Formation and the Carboniferous Epen Formation in the Netherlands. *Criticial assessment of shale plays,* Volume 103, pp. 1-24.

Bonnet, E., Bour, O., Odling , N. & Davy, P., 2001. Scaling of fracture systemes in geological media. *Geophysic,* 39(3), pp. 347-383.

Bour, O. & Davy, P., 1999. Clustering and size distributions of fault patterns:theory and measurements. *Geophysical research letters,* 26(13), pp. 2001-2004.

Brune, J., 1970. Tectonic stress and the spectra of seismic shear waves from earthquakes. *Geophysical research ,* 75(26), p. 4997=5010.

Bruns, B. et al., 2016. Thermal evolution and shale gas potential estimation of theWealden and Posidonia Shale in NW-Germany and the Netherlands: a 3D basinmodelling study. *Basin Research,* pp. 2-33.

Cho, D. & Perez, M., 2014. Brittleness revisited. *GOCUS.*

Civian, F., Rai, C. & Sondergeld, C., 2011. Shale-Gas Permeability and Diffusivity Inferred by Improved Formulation of Relevant Retention and Transport Mechanisms. *Transp porous med,* Volume 86, pp. 925-944.

Davies, R., Foulger, A., Bindley, A. & Styles, P., 2013. Induced Seismicity and Hydraulic Fracturing for the Recovery of Hydrocarbons. *Physical and Geographical Sciences,* pp. 2-60.

Di Tioro, G. et al., 2011. Fault lubrication during earthquakes. *Nature,* Volume 471, p. 494–498.

Eaton, D., Davidsen, J., Pedersen, K. & Boroumand, N., 2014. Breakdown of the Gutenberg-Richter relation for microearthquakes induced by hydraulic fracturing: influence of stratabound fractures. *Geo-prospecting,* Volume 62, pp. 806-818.

Eckert, A., 2007. 3D multi-scale finite element analysis of the crustal state of stress in the Western US and the Eastern California Shear Zone, and implications for stress – fluid flow interactions for the Coso Geothermal Field. *DISSERTATION.*

Economides, m. & Boney, C., 2000. Reservoir stilumation in petroleum production. *Reservoir stimulation,* pp. 1-1.

Eisner, L. et al., 2010. Beyond the dots in the box - Microseismicity-Constrained Fracture Models for Reservoir Simulation. *Microseismic Inc., Houston, USA,* Volume 2010, pp. 1-4.

Fang, Y., Elsworth, D., Trenton, T. & Cladouhos, T., submitted. Reservoir permeability mapping using microearthquake data. *Energy and engineering,* pp. 1-30.

Fatehi Marji, M., Pashapour, A. & Gholamnejad, J., 2011. Relationship between fracture dip angle, aperture and fluid flow in the fractured rock masses. *Journal of Mining & Environment,* 2(2), pp. 136-145.

Fischer, T. & Guest, A., 2011. Shear and tensile earthquakes caused by fluid injection. *Geophysical research letters,* Volume 38, pp. 1-4.

Franchi, J. R., 2008. Directional Permability. *Colorado school of mines,* pp. 565-569.

Gale, J., Reed, R. & Holder, J., 2007. Natural fractures in the Barnett Shale and their importance for hydraulic fracture treatments. *APPG,* 93(4), pp. 603-622.

Gaucher, E. et al., 2015. Induced siesmicity in Geothermal reservoirs: Physical Processes and key parameters. pp. 19-25.

Geng, Z. et al., 2016. Integrated Fracability assessment methodology for unconventional naturally fractured reservoirs: Bridging the gap between geophysics and production. *Petrolemum Science and Engineering,* pp. 640-647.

Gillespie, P., Walsh, J. & Watterson, J., 1996. Limitations of dimension and displacement data from single faults and consequaences for data analysisand interpretation. *Journal of structural geology,* Volume 14, p. 1157–1172.

Goertz-Allmann, B. et al., 2015. Combining microseismic and geomechanical observations to interpret storage integrity at the In Salah CCS site. *GJI Seismology,* Volume 198, p. 447–461.

Golf-Racht, T., 1982. *Fundamentals of fractured reservoir engineering.* 1 ed. Amsterdam: Elsevier.

Grieser, B. & Bray, J., 2007. Identification of production potential in Unconventional gas reservoirs. *SPE,* pp. 1-6.

Gutenburg, B. & Richter, C., 1944. Frequency of earthquakes in california. *Geophysics,* pp. 73-131.

Gutierrez, M., Oilno, L. & Nygard, R., 2000. Stress-dependent permeability of a de-mineralised fracture in Shale. *Marine and petroleum geology,* pp. 895-907.

Hammack, R. et al., 2014. An evaluation of fracture growth and gas/fluid migration as horizontal Marcellus Shale gas wells are hydraulically fractured in Greene County. *U.S Energy department,* pp. 1-80.

Herber, R. & de Jager, J., 2010. Oil and Gas in the Netherlands – Is there a future?. *Netherlands Journal of Geosciences,* pp. 91-107.

Hofmann, H. & Babadagli, T., 2013. Numerical Simulation of Complex Fracture Network Development by Hydraulic Fracturing in Naturally Fractured Ultratight Formations. *Offshore and Artic engineeering,* Volume 32, pp. 9-14.

Holditch, S., Jennings, J. & Neuse, S., 1978. The Optimation of Well Spacing and Fracture Length in Low Permeability Gas Reservoirs.. *SPE,* pp. 1-3.

Janzen, M., 2011. Hydraulic Fracturing in the Dutch Posidonia. *MSc Thesis,* pp. 12-43.

Javadpour, J., 2010. Nanopores and Apparent Permeability of Gas Flow in Mudrocks (Shales and Siltstones). *Journal of Canadian petrophysics,* pp. 16-24.

Jiang, X. et al., 2009. Estimation of fracture normal stiffness using atransmissivity-depth correlation. *Rock Mechanics & Miing Sciences ,* Volume 46, pp. 51-58.

Johri, M., Hennihgs , P. & Zoback, M., 2015. A scaling law to characterize fault-damage zones at reservoir depths. *AAPG,* 98(10), pp. 2057-2079.

Kim, Y. & Sanderson, D., 2005. The relationship between displacement and length of faults: A review. *Earth-Science Reviews,* Volume 68, p. 317–334.

King, E., 2010. Thirty years of gas shale fracturing: what have we learned ?. *SPE,* pp. 1-50.

Klimczak, C., Schultz, A., Parashar, R. & Reeves, D., 2010. Cubic law with aperture-length correlation: implications for network scale fluid flow. *Hydrogeology Journal,* Volume 18, p. 851–862.

Kumagai, H., Maeda, Y., Kame, M. & Kusakabe, T., 2014. Seismic moment and volume change of a spherical source. *Earth, plamnets and space,* 66(7).

Lei, G. et al., 2015. Calculation of full permeability tensor for fractured anisotropic media. *Petrol Explor Prod Technol,* Volume 5, pp. 167-176.

Mace, L., Souche, L. & MalleT, j., 2004. 3D Fracture Modeling Integrating Geomechanics and Geological Data. *AAPG,* Volume 1, pp. 24-27.

Marrett, R. & Allmendiger, R., 1991. Kinematic analysis of fault slip data. *Journal of stuctural Geology,* Volume 13, pp. 735-738.

Maxwell , S. et al., 2009. Imaging seismic deformation induced by hydraulic fracture complexity. *SPE,* Volume 1, p. 48–52.

Mayer & Associates , 2011. *Meyer fracturing simulators.* 9th ed. U.S.A: s.n.

McGarr, A., 1976. Seismic Moments and Volume Changes. *Journal of Geophysical Research,* 81(8), pp. 1487-1495.

McGarr, A., 2014. Maximum magnitude earthquakes induced by fluid injection. *AGU,* pp. 1008-1019.

Moeck, I., Kwiatek, G. & Zimmermann, G., 2009. Slip tendency analysis, fault reactivation potential and induced seismicity in a deep geothermal reservoir. *Journal of Structural Geology,* 31(10), pp. 1174-1182.

Mohaghegh, S., Arefi, S., Ameri, S. & Rose, D., 1994. Design and Development of an Artificial Neural Network for Estimation of Formation Permeability. *SPE,* pp. 1-5.

Nasirisavadkouhi, A., 2015. A Comparison Study of KGD, PKN and a Modified P3D Model. *Spring .*

Nicol, A., Walsh, J., Watterson, J. & Gillespie, J., 1996. Fault size distributions m are they really power-law?. *Journal of Structural Geology,* 18(2/3), pp. 191-197.

Nicol, J., Walsh, J., Watterson, K. & Gillespie, P., 1996. Fault size distributions m are they really power-law?. *Journal of structural geology,* 18(2/3), pp. 191-197.

Osinga, S., Wassing, B. & Heege, J., 2015. Induced seimicity related to globa; shale gas operations; A review. *M4ShaleGas.*

Passey, R. et al., 1990. A practical Model for organic Richness from Porosity and Resistiviy Logs. *Amercicam association of petroleum Geologists,* Volume 19, pp. 1777-1794.

Ramsey, J. & Chester, F., 2004. Hybrid fracture and the transition from extension fracture to shear fracture. *Nature,* pp. 77843-3115.

Randall, M., 1971. Shear invarient and siemic moment for deep ofcus earthquakes. *Geophysical research,* Volume 76, pp. 4991-4992.

Rickman, R. et al., 2008. A practical use of shale petrophysics for stimulation design optimization: All shale plays are not clones of the Barnett Shale. *SPE.*

Rutqvist, J. et al., 2008. Analysis ofthermallyinducedchangesinfracturedrockpermeability during 8yearsofheatingandcoolingattheYuccaMountain Drift ScaleTest. *International JournalofRockMechanics&MiningSciences,* Volume 25, pp. 1373-1389.

Rutter, H., Mecklenburgh, J., Mckaren, R. & Taylor, R., 2015. Pressure-dependent Permeability of Shales. *Fault and top seals,* pp. 1-9.

Schlische, R., Young, S. & Ackerman, R., 1996. Geometry and scaling relations of a population of very small rift-related normal faults. *Geology,* 24(8), pp. 683-686.

Scholz, C. & Cowie, P., 1990. Determination of total strain from faulting using slip measurments. *Nature,* Volume 346, pp. 837-839.

Segall, P. & Lu, S., 2015. Injection-induced seismicity: Poroelastic and earthquake nucleation effects. *Journal of Geoophysical Research.*

Shapiro, S., Dinske, C. & Langenbruch, C., 2010. Seismogenic index and magnitude probability of earthquakes induced during reservoir fluid stimulations. *Micro Seismic,* Volume 1, pp. 936-940.

Speight, J., 2017. *Deep shale oil and gas.* 1 ed. Cambridge`: Oxford.

Taron, J., Elsworth, D. & Min, K., 2009. Numerical stimulation of thermal-hydrologic-mechanical-chemical processes in deformable, fractured porous media. *Rock mechanics and mining services,* pp. 842 - 854.

Ter Heege, J. et al., 2015. Sweet spot identification in underexplored shales using multidisciplinary reservoir characterization and key performance indicators: Example of the Posidonia Shale Formation in the Netherlands. *Journal of Natural Gas Science and Engineering,* Volume 27, pp. 558-557.

TerHeege, J., 2016. Distribution and properties of faultsd and fractures in shales: Permeability model and implcations for optimum flow atimulation by hydraulic fracturing. *Petroleum Geosciences.*

TerHeege, J. H., 2016. Distribution and properties of faults and fractures in shales: Permeability model and implications for optimum flow stimulation by hydrofracturing. *American rock mechanics association,* pp. 1-9.

Van Bergen, J., Zijp, M., Nelskamp, S. & Kmobrink, H., 2013. Shale Gas Evaluation of the Early Jurassic Posidonia Shale Formation and the Carboniferous Epen Formation in the Netherlands. *Critical assessment of shale resource plays,* pp. 1-24.

Verdon, J., Kendall, J., White, D. & Angus, D., 2011. Linking microseismic event observations with geomechanical mod3els to minime the risks of storing Co2 in geological formations. *Earth and Planetary Science Letters,* pp. 143-452.

Wang, F. & Gale, F. W., 2009. Screenibg Criteria for Shale Gas Systems. *Economic Geology.*

Wang, Y., Li, X. & Zhang, B., 2016. Numerical Modeling of Variable Fluid Injection-Rate Modes on Fracturing Network Evolution in Naturally Fractured Formations. *energies,* Volume 9, pp. 414-432.

Wassing, B., van Wees, J. & Fokker, P., 2014. Coupled continuum modelingof fracture reactivation and induced seismicity during enhanced geothermal operations. *Geothermics,* Volume 52, pp. 153-164.

Wojatal, S., 1996. Dsiplacement correlated to linkage between faults. *Journal of Sturctural geology,* 1(1), pp. 260-275.

Wojtal, S., 1996. Changes in fault displacment populations coreelated to linkage between faults. *Pergamon,* 18(2/3), pp. 265-279.

Yielding, G., Needham, T. & Jones, H., 1996. Sampling of fault populations using sub-surface data: a review. *Journal of structural geology,* 18(2/3), pp. 135-146.

Zhu, Y. & Wilson, T., 2016. Variations of microseimic b-values and their relationship to 3D seismic structure in the Marcellus Shale: Southwestern Pennsylvania. *SEG,* pp. 2046-2050.

Zijp, M., Nelskamp, S., Verreuessel, R. & Heege, J., 2015. The Geverik member of the Carboniferous Epen Formation, Shale gas potential in Western Europe. *International petroleum energy conference,* pp. 1-9.

Appendix

Appendix 1

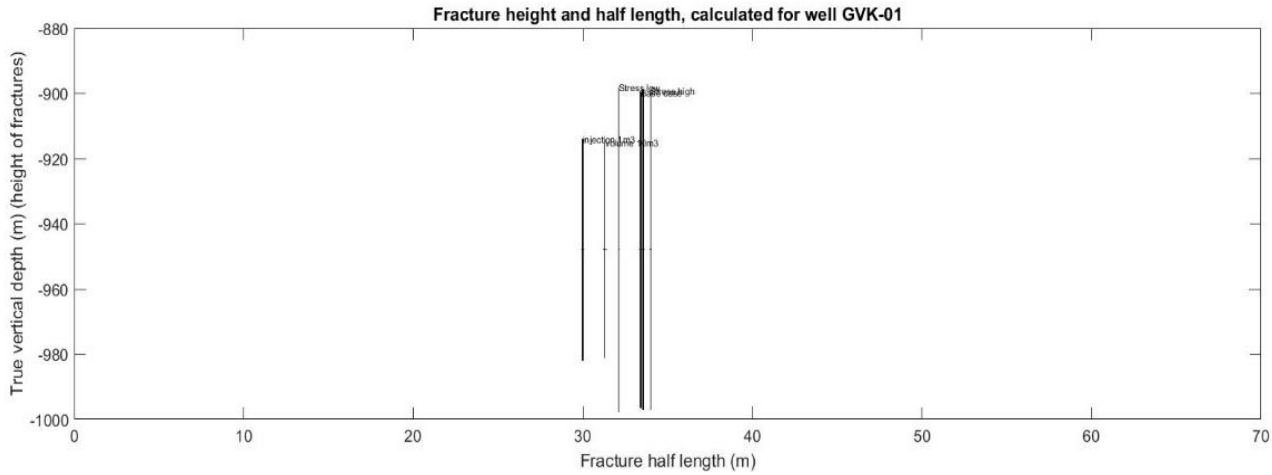

a

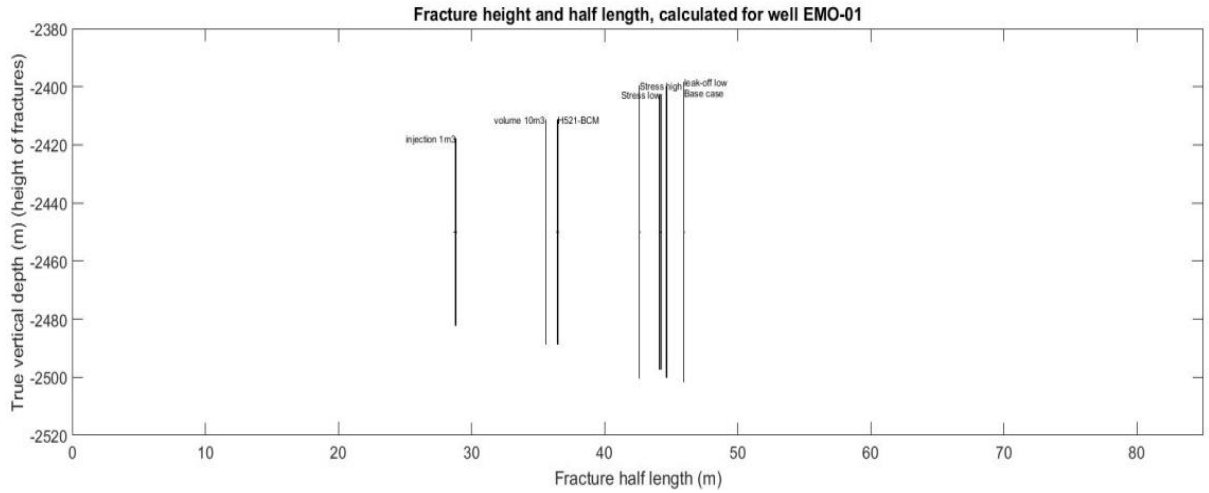

b

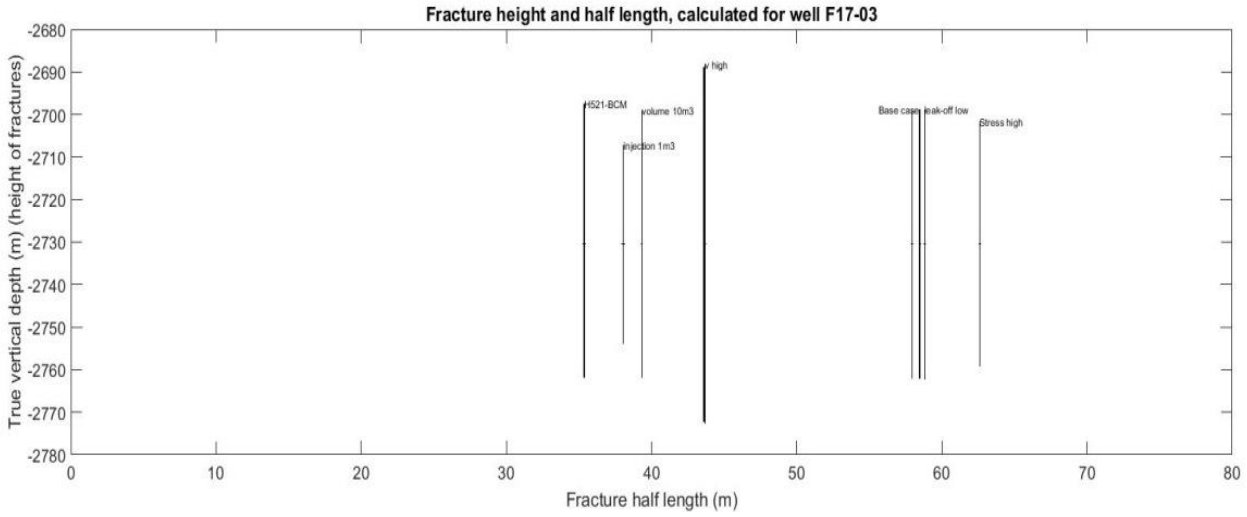
Fracture height and half length, calculated for well F17-03
True vertical depth (m) (height of fractures)
Fracture half length (m)
v high
H521-BCM
volume 10m3
injection 1m3
Base case
leak-off low
Stress high

c

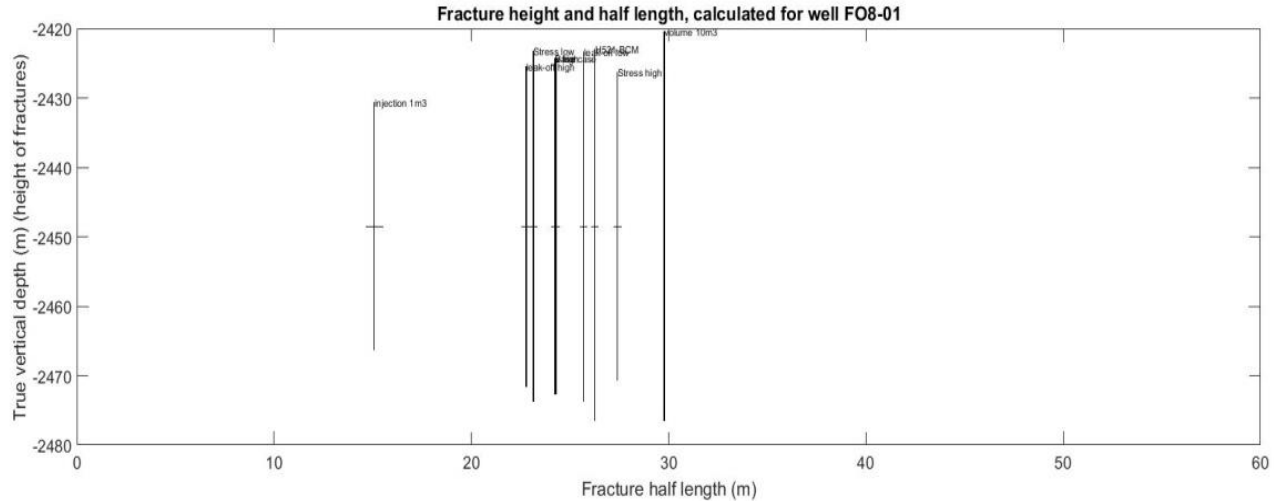
Fracture height and half length, calculated for well FO8-01
True vertical depth (m) (height of fractures)
Fracture half length (m)
volume 10m3
injection 1m3
Stress high

d

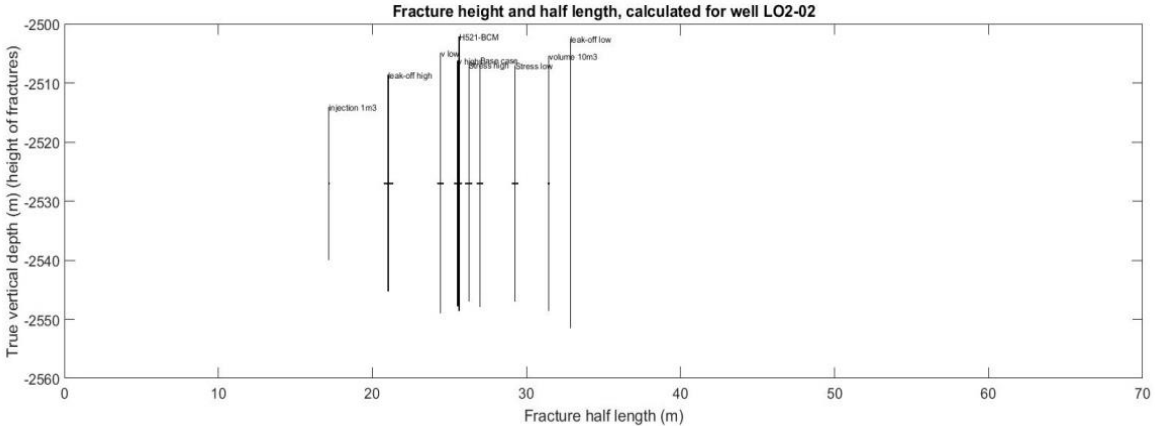
Fracture height and half length, calculated for well LO2-02
True vertical depth (m) (height of fractures)
Fracture half length (m)
H521-BCM
leak-off low
leak-off high
volume 10m3
injection 1m3
Stress low

e

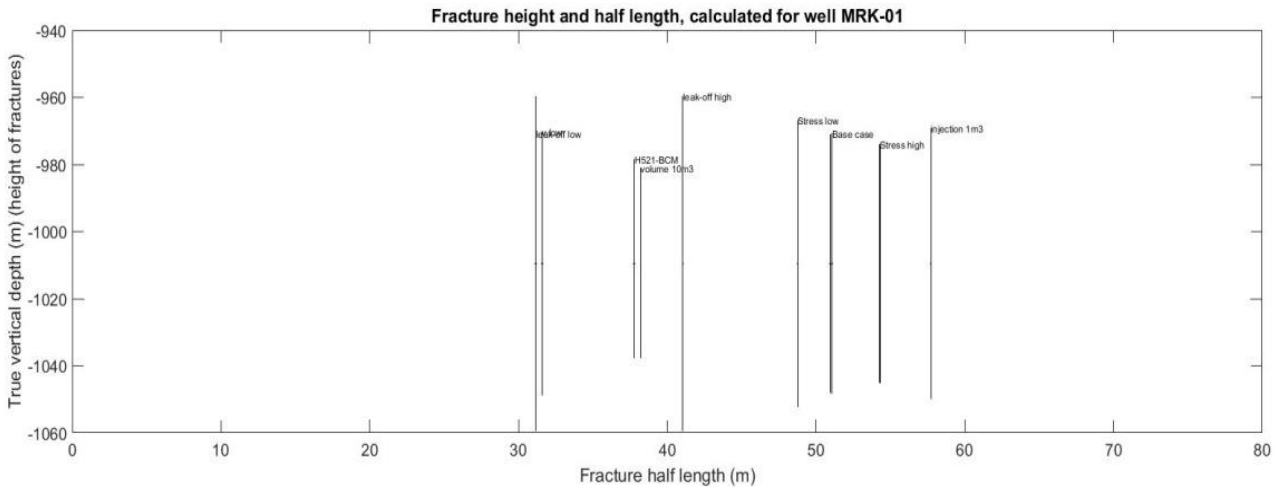
Fracture height and half length, calculated for well MRK-01
True vertical depth (m) (height of fractures)
Fracture half length (m)
-940
-960
-980
-1000
-1020
-1040
-1060
0
10
20
30
40
50
60
70
80
leak-off high
Stress low
Base case
Stress high
injection 1m3
H521-BCM
volume 10m3

f

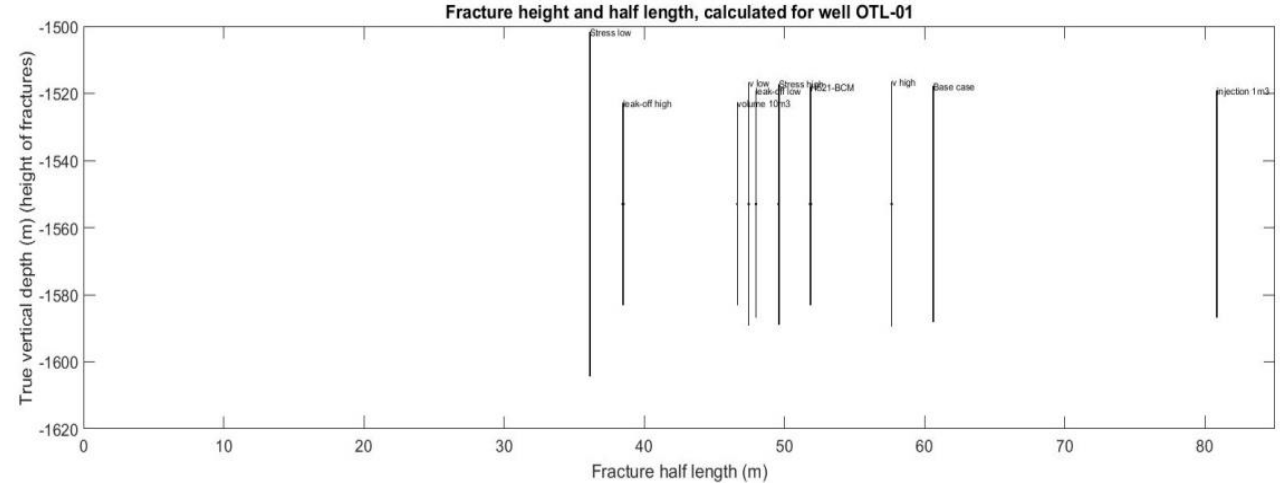
Fracture height and half length, calculated for well OTL-01
True vertical depth (m) (height of fractures)
Fracture half length (m)
-1500
-1520
-1540
-1560
-1580
-1600
-1620
0
10
20
30
40
50
60
70
80
Stress low
leak-off high
Base case
injection 1m3
H521-BCM
volume 10m3

g

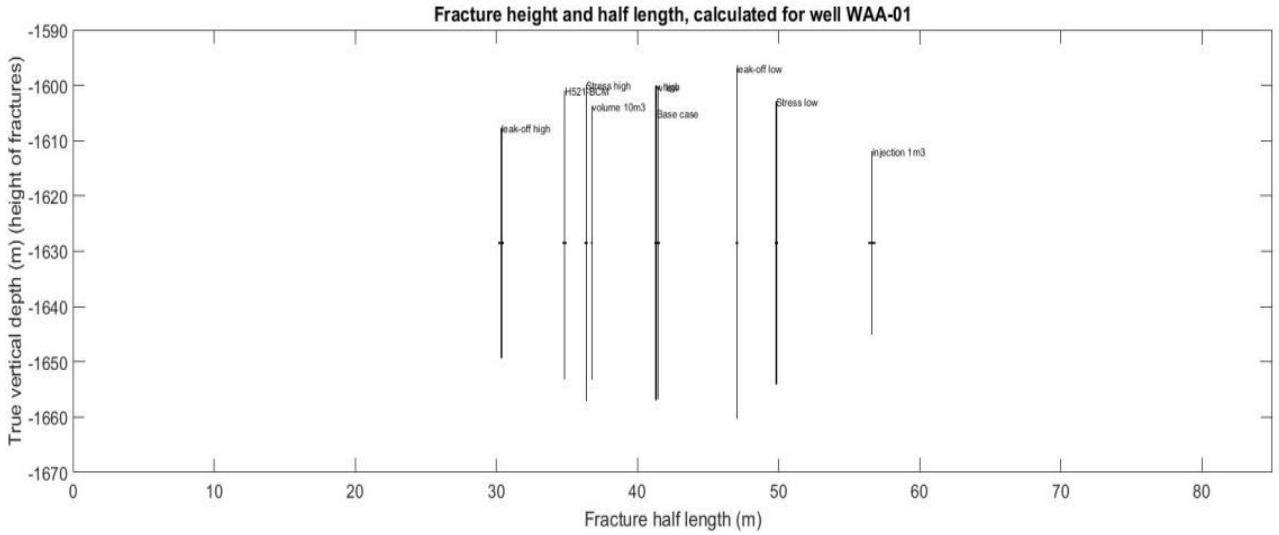
Fracture height and half length, calculated for well WAA-01
True vertical depth (m) (height of fractures)
Fracture half length (m)
-1590
-1600
-1610
-1620
-1630
-1640
-1650
-1660
-1670
0
10
20
30
40
50
60
70
80
leak-off high
leak-off low
Stress low
Base case
injection 1m3
H521-BCM
volume 10m3

h

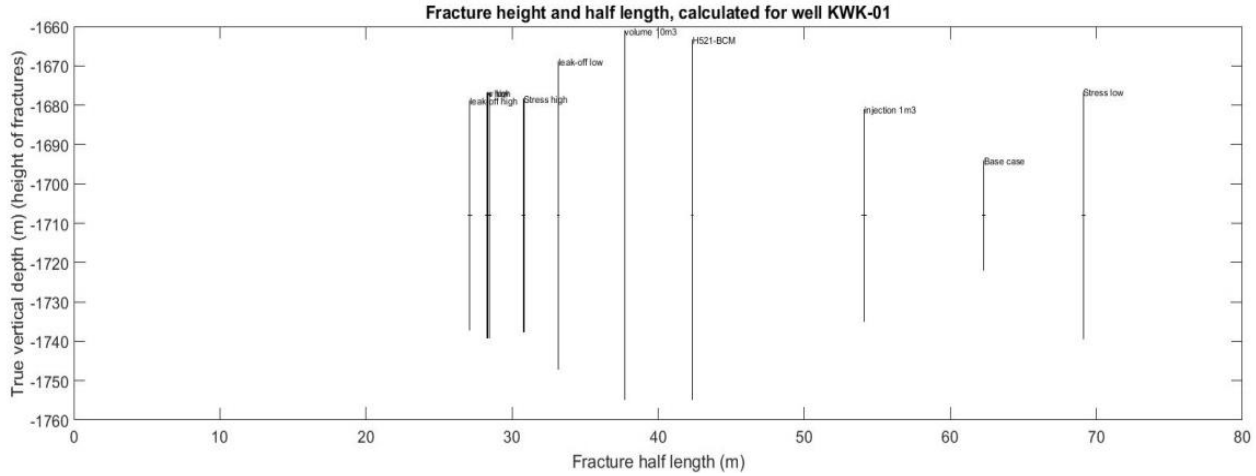

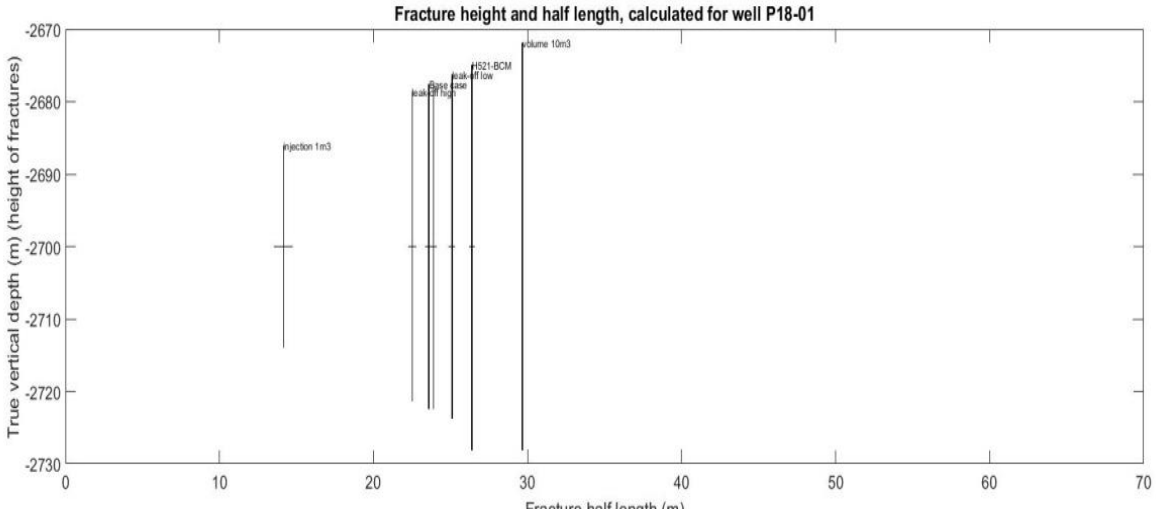

I

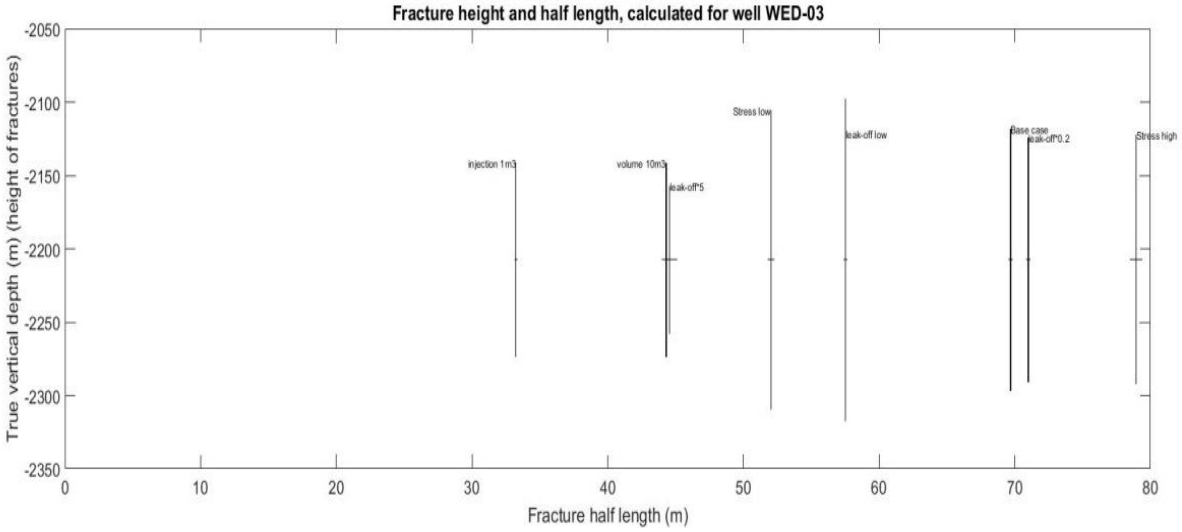

Figure 26 collection of MFrac results from all the wells considered in this study.

Appendix 2

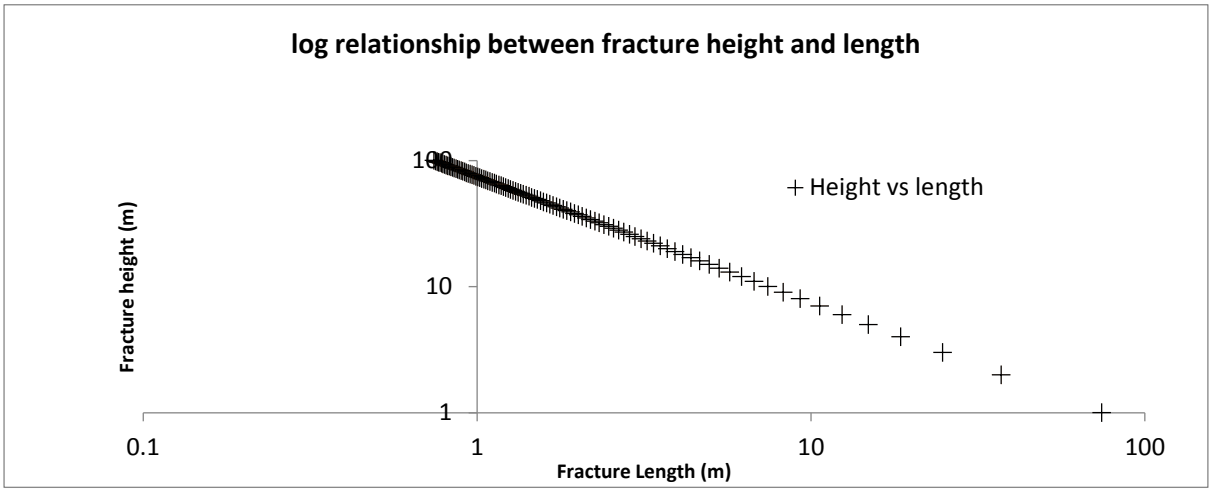

Figure 27 Plot depicts an analytical approach to highlighting the relationship between height and length of fractures using equation 12.

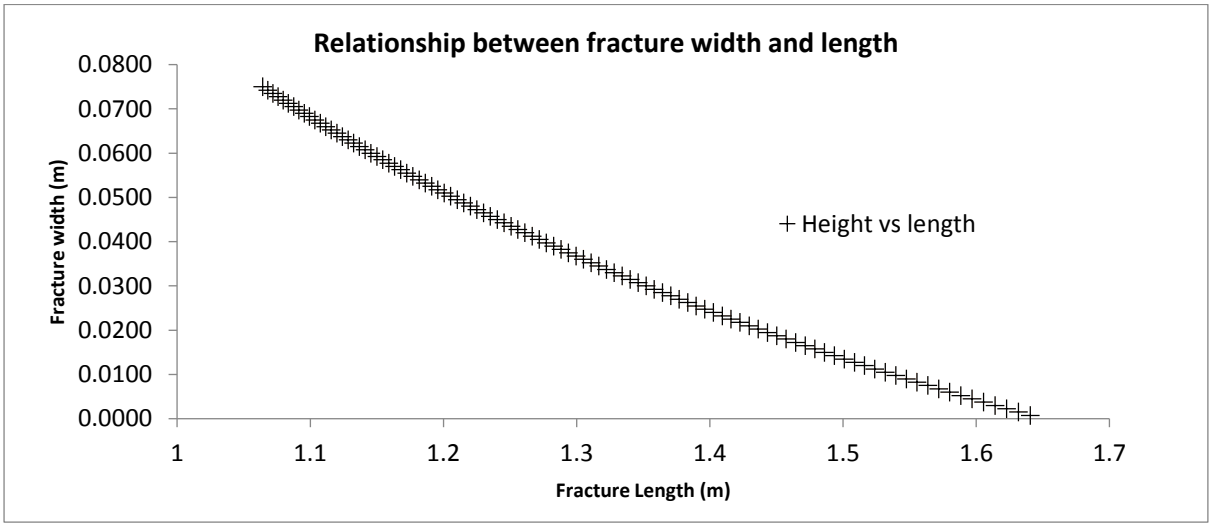

Figure 28 Shows the relationship between fracture width and length where fracture height was held constant and width could vary from 1 to 100 mm. calculated with equation 12.

Appendix 3

Table 5. Table listing the TOF, E, v and stress conditions at each well

Wells	Thickness (meters)	mean v	mean E	TOC (%)	Shmin	BI ratio
EMO-01	2450	0.24722	38.43441	5.11	37.6	19.3
WED-03	2208	0.320324	12.18796	3.2	39.1	6.2
MRK-01	1010	0.236175	38.28006	6.8	14.2	19.2
KWK-01	1708	0.245352	34.17603	7.9	24.4	17.2

OTL-01	1553	0.279892	19.60469	12.38	25.1	9.9
WAA-01	1628.5	0.262561	20.77885	5.07	23.6	10.5
WLK-01	1010	0.281458	38.28006	12.5	15.2	19.2
F17-03	2730.5	0.259769	22.69491	5.81	34.0	11.5
P18-02	2700	0.282425	18.59605	1.25	44.0	9.4
L02-02	2527	0.244692	38.05098	12.8	36.9	19.1
F08-01	2448.5	0.24017	42.78874	4.86	36.9	21.5
GAG-01	2915	0.24787	117.331	1.2	43.7	58.7

(Goertz-Allmann, et al., 2015)